LBNL-42486
Preprint

ERNEST ORLANDO LAWRENCE
BERKELEY NATIONAL LABORATORY

Imaging the Alignment Angular Distribution: State Symmetries, Coherence Effects and Nonadiabatic Interactions in Photodissociation

Allan S. Bracker, Eloy R. Wouters, Arthur G. Suits,
and Oleg S. Vasyutinskii

Chemical Sciences Division

October 1998

Submitted to
Journal of Chemical Physics

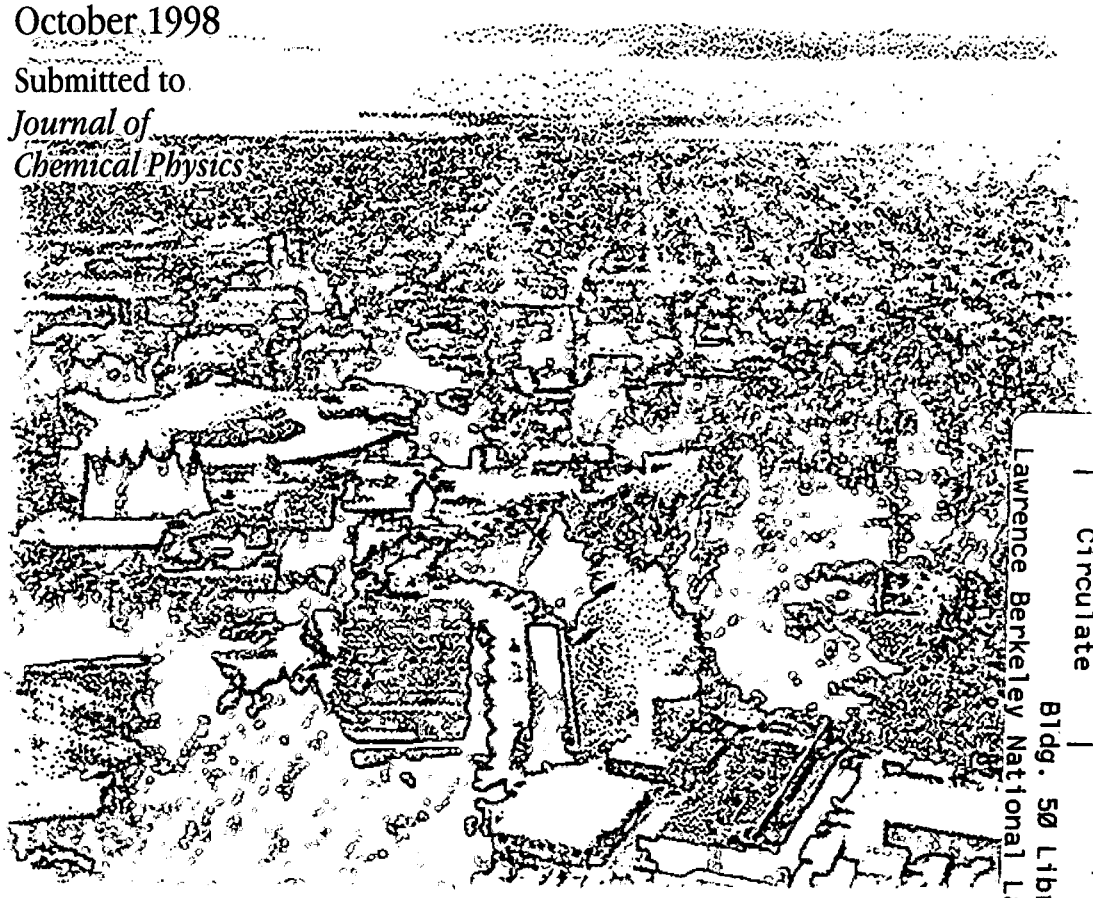

DISCLAIMER

LBNL-42486

Imaging the Alignment Angular Distribution: State Symmetries, Coherence Effects and Nonadiabatic Interactions in Photodissociation

Allan S. Bracker,[a,b,*] Eloy R. Wouters,[b] and Arthur G. Suits,[b,†]

[a]Department of Chemistry
University of California, Berkeley, California 94720
[b]Chemical Sciences Division
Ernest Orlando Lawrence Berkeley National Laboratory
Berkeley, California 94720

Oleg S. Vasyutinskii[†]

Ioffe Physico-Technical Institute, Russian Academy of Sciences,
194021 St. Petersburg, Russia

October 1998

*Current address: Naval Research Laboratory, 4555 Overlook Avenue SW, Washington, DC 20375
[†]Corresponding authors

This work was supported by the Director, Office of Energy Research, Office of Basic Energy Sciences, Chemical Sciences Division, of the U.S. Department of Energy under Contract No. DE-AC03-76SF00098, and by a Cooperative Grant from the Civilian Research and Development Foundation, CRDF Award No. RP1-223.

Submitted to JCP

Imaging the alignment angular distribution: State symmetries, coherence effects and nonadiabatic interactions in photodissociation.

Allan S. Bracker[a,b,*], Eloy R. Wouters[b] and Arthur G. Suits[b,†]
[a] *Department of Chemistry, University of California, Berkeley, CA 94720*
[b] *Chemical Sciences Division, Ernest Orlando Lawrence Berkeley National Laboratory, Berkeley, CA 94720*

Oleg S. Vasyutinskii[†]
Ioffe Physico-Technical Institute, Russian Academy of Sciences, 194021 St. Petersburg, Russia
(October 14, 1998)

Abstract

We establish a rigorous theoretical connection between measurements of the angular distribution of atomic photofragment alignment and the underlying dynamics of molecular photodissociation. We derive laboratory and molecular-frame angular momentum state multipoles as a function of photofragment recoil angles. These state multipoles are expressed in terms of *alignment anisotropy parameters*, which provide information on state symmetries, coherence effects, and nonadiabatic interactions. The method is intended for analysis of experimental data obtained with two-photon spectroscopy and ion imaging techniques, although it is readily modified for treating Doppler or ion time-of-flight profiles. We have applied this method to the photodissociation of Cl_2 at 355 nm, where we observe strong alignment in the ground state chlorine atom photofragments. Our analysis demonstrates that there are strong contributions to the alignment from both incoherent and coherent perpendicular excitation. We also show that the existence of atomic alignment due to coherence requires that nonadiabatic transitions occur at long range.

PACS numbers: 33.80.Gj, 34.50.Gb, 34.50.Lf

*Current address: Naval Research Laboratory, 4555 Overlook Ave, SW, Washington, DC 20375

†Corresponding authors

I. INTRODUCTION

Investigations of atomic photofragment polarization in photodissociation can yield deep insight into fundamental physical processes. The atomic angular momentum can be both oriented and aligned, corresponding to nonequilibrium populations of the m and $|m|$ magnetic sublevels, respectively [1,2]. As early as 1928, in a study of NaI photodissociation, Mitchell assumed that the atomic fragments could be polarized [3]. In 1968, Van Brunt and Zare first discussed a mechanism for this effect, and predicted that electronically excited photofragments could give rise to polarized fluorescence. They showed that atomic polarization would result from conservation of the projection of the total molecular angular momentum on the bond axis ($\Omega_{AB} = |m_A + m_B|$) during dissociation [4]. Experimental observation of atomic photofragment polarization dates to 1980, including reports of oriented ground state Cs($^2S_{1/2}$) atoms from CsI dissociation [5,6] and aligned excited state Na($^2P_{3/2}$) atoms from Na_2 dissociation [7]. The basic features of this phenomenon can be understood from a simple molecular orbital view of chemical bonding, which emphasizes the critical role played by the excited state symmetry. However, a more complete description must also address the role of coherence effects, nonadiabatic effects, and long-range interactions between the photofragments [8–17].

Although the early studies reported only the total angular momentum polarization, recent experimental developments have allowed measurement of the *recoil angle dependence* of the electronic angular momentum polarization (atomic **v**–**J** correlation). These studies used Doppler [18], ion time-of-flight [19,20], or ion imaging [21–24] methods, in combination with optical spectroscopy. The atomic **v**–**J** correlation is related in general to the analogous property for diatomic rotational angular momentum, which has been the focus of considerable interest since the late 1980s (see, for instance the reviews [25,26]). However, in most essential details, there is little similarity between atomic and molecular photofragment polarization phenomena. While semiclassical methods [27] are perfectly suitable for treating the large J cases typical for rotational angular momentum polarization, such methods are not appropriate for atomic polarization. Some general quantum mechanical treatments of the **v**–**J** correlation exist [28,29], but they have not addressed the physical origins of atomic photofragment polarization. Indeed, atomic and molecular photofragment polarization reflect very different aspects of the photochemical event. Rotational angular momentum polarization provides information on the shape of the potential energy surface, whereas the study of electronic polarization in atoms directly probes the electronic structure and dynamics, which determine the "fabric" of the potential energy surface.

Recently, a fully quantum mechanical theoretical treatment [30] has established the connection between the recoil angle dependence of atomic photofragment polarization and the detailed physics of the dissociation process. The work provides a critical link to the underlying details of the dissociation dynamics. However, full exploitation of the power of these results requires an additional theoretical link to recent experimental observations. The purpose of this paper is to make this connection—first quite generally, then with specific application to our ion imaging results for the 355 nm photodissociation of molecular chlorine. Ref. [30] shows that parallel and perpendicular optical excitations and coherence effects each have a unique influence on the angular distributions of orientation and alignment, and others have described how to include nonadiabatic effects in this formalism (see

e.g. Ref. [15]). Here, we connect these theoretical descriptions with observable features of ion imaging measurements.

The organization of the paper is as follows. In Sec. II, we present the theory of two-photon ion imaging spectroscopy of polarized atomic photofragments. First, the photofragment alignment state multipoles [30] are given in terms of alignment anisotropy parameters that can be directly determined from experiment. The transformation between the laboratory and recoil frame state multipoles is given, and the latter are shown to be related to unique dissociation mechanisms. Then the expressions describing two-photon absorption of light by atomic photofragments are presented and analyzed. These expressions are based on the analysis of Kummel, Sitz, and Zare [31,32], however they are adapted to the atomic case and given in somewhat different form. We show how combinations of signal from different experimental geometries can be used to obtain population-independent as well as alignment-independent contributions to the total signal. In Sec. III, we present alignment image basis functions that can be used to simulate the alignment contribution to photofragment image data and to determine the alignment anisotropy parameters. Sec. IV addresses our experimental study of molecular chlorine photodissociation at 355 nm. Sec. V presents analysis of the experimental results based on the theoretical approach given in Sec. II and III. This analysis shows that the nascent ground state chlorine atom is strongly aligned. We also give a detailed assignment of the dominant incoherent and coherent optical excitation processes and subsequent nonadiabatic effects occuring at large internuclear distances.

II. THEORY: TWO-PHOTON ION IMAGING SPECTROSCOPY OF POLARIZED ATOMIC PHOTOFRAGMENTS

A. PHOTOFRAGMENT ALIGNMENT ANGULAR DISTRIBUTIONS

1. Laboratory Frame

We consider a molecular photodissociation which produces fragments A and B with angular momenta j_A and j_B, respectively. The differential excitation cross section matrix elements $\sigma^{(j_A)}_{m'm}(\theta,\phi)$ give the probability of photofragment A flying in a direction specified by the polar angles θ,ϕ with components m,m' of j_A along the space-fixed $\mathbf{Z}$ axis (see Fig. 1). The diagonal elements of the matrix ($m=m'$) give the probability of producing the fragment with a specific angular momentum j_A and component m, while the off-diagonal elements ($m\neq m'$) describe the coherence between states with different m quantum numbers [1]. The initial and the final total angular momenta of the molecule are J_i and J, respectively.

It is convenient to express the excitation matrix elements $\sigma^{(j_A)}_{m'm}(\theta,\phi)$ in terms of the angular momentum polarization cross sections $\sigma^{(j_A)}_{KQ}(\theta,\phi)$, which are spherical tensors of rank K and component Q [1,2,33]

$$\sigma^{(j_A)}_{KQ}(\theta,\phi)=\sum_{m',m}(-1)^{j-m}(2K+1)^{1/2}\begin{pmatrix} j_A & j_A & K \\ m & -m' & -Q\end{pmatrix}\sigma^{(j_A)}_{m'm}(\theta,\phi). \tag{1}$$

(In subsequent expressions, the superscript (j_A) will be dropped for convenience.) The photofragment differential cross section [Eq. (1)] for one-photon fragmentation, obtained

with first-order perturbation theory for electric dipole transitions in the axial recoil approximation, is [30,34]

$$\sigma_{KQ}(\theta,\phi) = \frac{3\sigma_0(2K+1)^{1/2}}{4\pi} \sum_{k_d,q_d,Q'} \sum_{q,q'} (-1)^{K+q'} E_{k_d q_d}(\mathbf{e}) \frac{f_K(q,q')}{f_0(0,0)+2f_0(1,1)} \times (2k_d+1)^{1/2} \begin{pmatrix} 1 & 1 & k_d \\ q' & -q & -Q' \end{pmatrix} D^{K*}_{QQ'}(\phi,\theta,0) D^{k_d}_{q_d Q'}(\phi,\theta,0), \quad (2)$$

where $\sigma_0 = \langle \sigma_{0,0}(\theta,\phi) \rangle$ is a zeroth-order fragmentation cross section integrated over angles θ and ϕ, $D^K_{QQ'}(\phi,\theta,0)$ are Wigner functions [35], and $E_{k_d q_d}(\mathbf{e})$ is an element of the polarization matrix of the dissociation light [2,33,36–38]. In principle, the multipole rank K ranges from $K = 0$ to $K = 2j_A$ [1,2], although usually the lowest order terms [$K = 0$ (photofragment density), $K = 1$ (orientation), and $K = 2$ (alignment)] are the predominant contribution to experimental signals (see Sec. II B). For our chlorine study, we only need expressions for the cross sections $\sigma_{KQ}(\theta,\phi)$ with $K = 0$ and $K = 2$, because the $j = 3/2$ atoms are limited to $K \leq 3$, while the probe geometries used in this study restrict the observable state multipoles to even ranks only.

The values $f_K(q,q')$ in Eq. (2) are *dynamical functions*, which contain all the information on the transition dipole moments and fragmentation dynamics. The indices q, q' are cyclic components of the molecular electric dipole moment with respect to the recoil axis. They can have only the values 0 or ± 1, corresponding to parallel or perpendicular electronic transitions. The case $q \neq q'$ corresponds to simultaneous coherent excitation of different Ω, Ω' continua [39,40]. The dynamical functions are defined by

$$f_K(q,q') = \sum_{\Omega_A,\Omega'_A} (-1)^{j_A+\Omega_A} \begin{pmatrix} j_A & j_A & K \\ -\Omega_A & \Omega'_A & q-q' \end{pmatrix} M_{j_A\Omega_i\Omega_A} (M_{j_A\Omega_i\Omega'_A})^*, \quad (3)$$

and they obey the symmetry relations

$$f_K(q,q') = (-1)^K f_K(-q,-q') = (-1)^{q-q'} f^*_K(q',q). \quad (4)$$

The values $M_{j\Omega_i\Omega_A}$ are transition dipole matrix elements. In the semiclassical approximation and for the case when the Coriolis nonadiabatic interactions in the decaying molecules can be neglected, these values are [15]

$$M_{j_A\Omega_i\Omega_A}(M_{j_A\Omega_i\Omega'_A})^* = \sum T^{n\Omega^*}_{j_A\Omega_A\ j_B\Omega_B} T^{n'\Omega'}_{j'_A\Omega'_A\ j_B\Omega_B} N^{n_e\Omega\ n'_e\Omega'}_{n\Omega\ n'\Omega'} \times \langle \Phi_i(R)|\Phi_\Omega(R)\rangle \langle \Phi_i(R)|\Phi_{\Omega'}(R)\rangle^* \langle \Omega_i|d_q|n_e,\Omega\rangle \langle \Omega_i|d_{q'}|n'_e,\Omega'\rangle^*. \quad (5)$$

The indices Ω_A, Ω'_A, Ω_B, Ω_i, Ω, Ω' in Eqs (3) and (5) are the components of the angular momenta j_A, j_B, J_i, J onto the recoil axis, with $\Omega = \Omega_i - q$, $\Omega' = \Omega_i - q'$, $\Omega = \Omega_A + \Omega_B$, and $\Omega' = \Omega'_A + \Omega_B$. The indices n_e, n'_e, n, n' are the set of all other molecular quantum numbers and R is an internuclear separation. Subscript e refers to the optically-excited state(s) (*i.e.* prior to nonadiabatic transitions). The summation in Eq. (5) is over all repeated indices. All functions on the right hand side have a clear physical interpretation. The values $\langle \Omega_i|d_q|n_e,\Omega\rangle$ are the molecular dipole moment matrix elements. The values $\langle \Phi_i(R)|\Phi_\Omega(R)\rangle$

are Frank-Condon overlap integrals. Matrix elements $N^{n_e\Omega\ n'_e\Omega'}_{n\Omega\ n'\Omega'}$ describe all homogeneous nonadiabatic transitions ($\Delta\Omega = 0$, see *e.g.* Ref. [41]) between the adiabatic continua $n_e\Omega$ and $n\Omega$ [42]. Elements of matrices T are expansion coefficients of the molecular wavefunction over the separated fragment basis in the asymptotic region (internuclear distance $R \rightarrow \infty$) and describe long-range interactions between the fragments [16].

We first consider the photofragment polarization cross sections [Eq. (2)] in the laboratory frame. It is more convenient to work with the fragment state multipoles $\rho_{KQ}(\theta,\phi)$, obtained by normalizing $\sigma^j_{KQ}(\theta,\phi)$ by the total zeroth-order fragmentation cross section σ_0, which is proportional to the total number of fragments. This yields

$$\rho_{KQ}(\theta,\phi) = \frac{\sigma_{KQ}(\theta,\phi)}{(2j_A+1)^{1/2}\sigma_0}. \tag{6}$$

The fragment state mutipoles with $K = 2$ in Eq. (6) are related to the familiar fragment alignment parameters $A_{KQ}(\theta,\phi)$ by the well known transformation formula [2]

$$A_{2Q}(\theta,\phi) = \left[\frac{(2j_A+3)(2j_A-1)}{5j_A(j_A+1)}\right]^{1/2} \frac{\mathrm{Re}[\rho_{2Q}(\theta,\phi)]}{\rho_{00}(\theta,\phi)}. \tag{7}$$

It is also desirable to rewrite the expressions for $\rho_{2Q}(\theta,\phi)$ in terms of angle-independent alignment anisotropy parameters [18], which are normalized combinations of the dynamical functions. They are given by

$$\begin{aligned}
s_2 &= V(j_A)^{-1}\frac{f_2(0,0)+2f_2(1,1)}{f_0(0,0)+2f_0(1,1)} \\
\alpha_2 &= V(j_A)^{-1}\frac{f_2(1,1)-f_2(0,0)}{f_0(0,0)+2f_0(1,1)} \\
\gamma_2 &= 2\sqrt{3}V(j_A)^{-1}\frac{\mathrm{Re}[f_2(1,0)]}{f_0(0,0)+2f_0(1,1)} \\
\gamma'_2 &= 2\sqrt{3}V(j_A)^{-1}\frac{\mathrm{Im}[f_2(1,0)]}{f_0(0,0)+2f_0(1,1)} \\
\eta_2 &= \sqrt{6}V(j_A)^{-1}\frac{f_2(1,-1)}{f_0(0,0)+2f_0(1,1)},
\end{aligned} \tag{8}$$

where $V(j)=5\{j(j+1)/[(2j+3)(2j-1)]\}^{1/2}$.

The anisotropy parameters can be determined directly from experiment and give information about the dissociation dynamics. Parameters α_2, γ_2, and η_2 represent contributions to the total diagonal alignment parameter $\langle A_{20}\rangle$ [2,43] from different excitation mechanisms. Parameter α_2 describes the total alignment due to incoherent excitation ($q = q'$), via both parallel and perpendicular transitions. Parameter γ_2 describes aligment from a coherent superposition of parallel and perpendicular excitation. This parameter is important when two excited electronic states with electronic projections Ω equal to ± 1 and 0 have comparable excitation probabilities. Parameter η_2 relates to coherent superposition of two perpendicular transitions. This may occur for two states separated in energy as in the parallel/perpendicular case. However, a more common possibility is simultaneous excitation of the degenerate $\Omega = \pm 1$ "lambda doublet" components of an $|\Omega| = 1$ state (see

Ref. [12]), since both states automatically have equal excitation probabilities. By integrating the equation for $\rho_{20}(\theta,\phi)$ over recoil angles, one obtains

$$\langle A_{20}\rangle = \alpha_2 + \gamma_2 + \eta_2 \tag{9}$$

when the dissociation light is circularly polarized or unpolarized and propagates along the **Z** axis, and

$$\langle A_{20}\rangle = -2(\alpha_2 + \gamma_2 + \eta_2) \tag{10}$$

when the dissociation light is linearly polarized along the **Z** axis.

The parameters s_2 and γ_2' in Eq. (8) represent a contribution to the alignment components that vanishes after averaging over all recoil angles. The parameter s_2 describes a contribution to all alignment components $A_{2Q}(\theta,\phi)$ ($Q = 0, \pm 1, \pm 2$) due to incoherent excitation via both parallel and perpendicular transitions, while the parameter γ_2' corresponds to coherent superposition of parallel and perpendicular excitation that contributes only to off-diagonal alignment parameters $A_{2\pm1}(\theta,\phi)$, $A_{2\pm2}(\theta,\phi)$ when the dissociation light is circularly polarized (see Ref. [30]).

Using Eqs (2) and (6) and the definition of the alignment anisotropy parameters [Eq. (8)], we obtain expressions for the specific differential photofragment state multipoles. For completeness, we also include the well-known expression from Ref. [44] for the zeroth-order state multipole ρ_{00}.

Geometry I: Dissociation light is linearly polarized along the **Z** axis:

$$\begin{aligned}
\rho_{00}(\theta,\phi) &= \frac{1}{4\pi\sqrt{2j_A+1}}[1+\beta_0 P_2(\cos\theta)] \\
\rho_{20}(\theta,\phi) &= \frac{\sqrt{5}V(j_A)}{4\pi\sqrt{2j_A+1}}\Big\{P_2(\cos\theta)[s_2 - 2\alpha_2 P_2(\cos\theta)] - 3\gamma_2\sin^2\theta\cos^2\theta - \frac{3}{4}\eta_2\sin^4\theta\Big\} \\
\rho_{21}(\theta,\phi) &= -\frac{\sqrt{15}V(j_A)}{4\sqrt{2}\pi\sqrt{2j_A+1}}\sin\theta\cos\theta e^{i\phi}\Big\{[s_2 - 2\alpha_2 P_2(\cos\theta)] + \gamma_2(2\cos^2\theta - 1) \\
&\quad + \frac{1}{2}\eta_2\sin^2\theta\Big\} \\
\rho_{22}(\theta,\phi) &= \frac{\sqrt{15}V(j_A)}{8\sqrt{2}\pi\sqrt{2j_A+1}}\sin^2\theta e^{2i\phi}\Big\{[s_2 - 2\alpha_2 P_2(\cos\theta)] + 2\gamma_2\cos^2\theta - \frac{1}{2}\eta_2(1+\cos^2\theta)\Big\}
\end{aligned} \tag{11}$$

Geometry II: Dissociation light is linearly polarized along the **Y** axis:

$$\begin{aligned}
\rho_{00}(\theta,\phi) &= \frac{1}{4\pi\sqrt{2j_A+1}}[1 - \frac{\beta_0}{2}(1 - 3\sin^2\theta\sin^2\phi)] \\
\rho_{20}(\theta,\phi) &= \frac{\sqrt{5}V(j_A)}{4\pi\sqrt{2j_A+1}}\Big\{P_2(\cos\theta)\Big[s_2 + \alpha_2[P_2(\cos\theta)(1-\cos 2\phi) + \cos 2\phi]\Big] \\
&\quad + \frac{3}{2}\gamma_2\sin^2\theta\cos^2\theta(1-\cos 2\phi) \\
&\quad + \frac{3}{8}\eta_2\sin^2\theta[\sin^2\theta + (1+\cos^2\theta)\cos 2\phi]\Big\}
\end{aligned} \tag{12}$$

$$\rho_{21}(\theta,\phi) = -\frac{\sqrt{15}V(j_A)}{4\sqrt{2}\pi\sqrt{2j_A+1}}\sin\theta\cos\theta e^{i\phi}\Big\{\Big[s_2+\alpha_2[P_2(\cos\theta)(1-\cos 2\phi)+\cos 2\phi]\Big]$$
$$-\frac{\gamma_2}{2}[\cos 2\theta(1-\cos 2\phi)+i\sin 2\phi]$$
$$-\frac{\eta_2}{4}[(1-\cos 2\phi)\sin^2\theta+2\cos 2\phi-2i\sin 2\phi]\Big\}$$
$$\rho_{22}(\theta,\phi) = \frac{\sqrt{15}V(j_A)}{8\sqrt{2}\pi\sqrt{2j_A+1}}e^{2i\phi}\Big\{\sin^2\theta\Big[s_2+\alpha_2[P_2(\cos\theta)(1-\cos 2\phi)+\cos 2\phi]\Big]$$
$$-\gamma_2\sin^2\theta[\cos^2\theta(1-\cos 2\phi)+i\sin 2\phi]$$
$$+\frac{\eta_2}{4}[(1+\cos^2\theta)\sin^2\theta+(1+\cos^2\theta)^2\cos 2\phi-4i\cos^2\theta\sin 2\phi]\Big\}$$

The following relation holds in general:

$$\rho_{K-Q}(\theta,\phi) = (-1)^Q\rho^*_{KQ}(\theta,\phi). \tag{13}$$

The anisotropy parameter β_0 in $\rho_{00}(\theta,\phi)$ can be written in terms of dynamical functions as [30,45]

$$\beta_0 = \frac{2[f_0(0,0)-f_0(1,1)]}{2f_0(1,1)+f_0(0,0)}. \tag{14}$$

2. Molecular Frame

The power of ion imaging and other techniques that are used to measure the angular distribution of angular momentum polarization is that they readily lead to an understanding of the dynamics in the frame of the molecule. In order to examine the angular momentum polarization in the molecular frame (see Fig. 1), it is convenient to normalize the cross sections by the zeroth-order differential fragmentation cross section $\sigma_{00}(\theta,\phi)$, which is proportional to the number of fragments flying in the direction defined by the angles θ,ϕ. The expression for the molecular frame state multipoles $\rho^{mol}_{KQ'}(\theta,\phi)$ is given by

$$\rho^{mol}_{KQ'}(\theta,\phi) = \frac{\sigma_{KQ'}(\theta,\phi)}{(2j_A+1)^{1/2}\sigma_{00}(\theta,\phi)}, \tag{15}$$

where the indices Q' are the components of multipole rank K along the recoil axis $\mathbf{Z}'$. Using Eqs (6) and (15), one obtains the relationship between the laboratory and molecular frame state multipoles

$$\rho_{KQ}(\theta,\phi) = (2j_A+1)^{1/2}\rho_{00}(\theta,\phi)\sum_{Q'}D^{K*}_{QQ'}(\phi,\theta,0)(\rho^{mol}_{KQ'}), \tag{16}$$

where the zeroth-order laboratory frame multipole $\rho_{00}(\theta,\phi)$ is given in Eqs (11) and (12).

The relationships between the molecular frame state multipoles [Eq. (15)] and the alignment anisotropy parameters [Eq. (8)] are obtained using Eqs (6), (16), and (11):

$$\begin{aligned}
\rho_{00}^{mol} &= \frac{1}{\sqrt{2j_A+1}} \\
\rho_{20}^{mol} &= \frac{\sqrt{5}V(j_A)}{\sqrt{2j_A+1}} \frac{[s_2 - 2\alpha_2 P_2(\cos\theta)]}{[1+\beta_0 P_2(\cos\theta)]} \\
\mathrm{Re}[\rho_{21}^{mol}] &= -\frac{\sqrt{30}V(j_A)}{2\sqrt{2j_A+1}} \frac{\gamma_2 \sin\theta\cos\theta}{[1+\beta_0 P_2(\cos\theta)]} \\
\rho_{22}^{mol} &= -\frac{\sqrt{30}V(j_A)}{4\sqrt{2j_A+1}} \frac{\eta_2 \sin^2\theta}{[1+\beta_0 P_2(\cos\theta)]}.
\end{aligned} \tag{17}$$

If parallel and perpendicular optical transitions occur simultaneously, it is clear from Eq. (17) that to describe the photofragment alignment in the molecular frame, one needs three independent state multipoles ρ_{20}^{mol}, ρ_{21}^{mol}, and ρ_{22}^{mol}, which all depend on the angle θ. The state multipole ρ_{20}^{mol} is related to incoherent parallel and perpendicular transitions, while the multipoles ρ_{22}^{mol} and ρ_{21}^{mol} are related to coherent superposition of two perpendicular transitions or a parallel and a perpendicular transition, respectively. The multipoles ρ_{20}^{mol} and ρ_{22}^{mol} are real, while the multipole ρ_{21}^{mol} can be complex, although only its real part contributes to the photofragment alignment produced by linearly polarized or unpolarized light.

These state multipoles characterize the angular distribution of the molecular-frame angular momentum polarization. Each of them represents a component of the characteristic shape of the electron cloud in the recoiling atom, as shown in Fig. 2. Although the shapes are independent of recoil angle, their relative contributions are not, and this angular dependence is different for each state multipole. Thus in general, the shape of the electron cloud will vary with recoil direction.

In the limit of a pure perpendicular transition, $2\alpha_2 = s_2$ [see Eq. (8)], $\beta_0 = -1$ and $\gamma_2 = 0$. Only the state multipoles ρ_{20}^{mol} and ρ_{22}^{mol} in Eq. (17) are nonzero. They do not depend on the angle θ and have the values

$$\rho_{20}^{mol} = \frac{2\sqrt{5}V(j_A)}{\sqrt{2j_A+1}}\alpha_2; \qquad \rho_{22}^{mol} = -\sqrt{\frac{5}{6}}\frac{V(j_A)}{\sqrt{2j_A+1}}\eta_2. \tag{18}$$

Using Eq. (7), one can see that the expressions (18) correspond to the following values of the molecular frame photofragment alignment parameters: $A_{20}^{mol} = 10\alpha_2$, $A_{22}^{mol} = -5\eta_2/\sqrt{6}$. For a pure parallel transition, $\alpha_2 = -s_2$ [Eq. (8)], $\beta_0 = 2$, $\gamma_2 = \eta_2 = 0$. Only the state multipole ρ_{20}^{mol} is nonzero and has the value

$$\rho_{20}^{mol} = -\frac{\sqrt{5}V(j_A)\alpha_2}{\sqrt{2j_A+1}}, \tag{19}$$

which corresponds to a molecular frame alignment parameter $A_{20}^{mol} = -5\alpha_2$.

Finally, it should be emphasized that all three laboratory frame state multipoles $\rho_{20}(\theta,\phi)$, $\rho_{21}(\theta,\phi)$, and $\rho_{22}(\theta,\phi)$ are nonzero. This is clear from Eqs (11) and (12) at the end of the previous section.

B. ABSORPTION OF LIGHT BY ATOMIC PHOTOFRAGMENTS

Kummel and coworkers have described a method for extracting orientation and alignment information from measurements which use two-photon excitation as a probe of diatomic photofragments [31,32]. We have adapted their approach for atoms and made some convenient modifications. The general expression describing the intensity of absorption of the probe light by the photofragments is

$$I = C \sum_{K k_1 k_2} S^{k_2}_{K k_1} \left[(\rho_K \otimes E_{k_1})_{k_2} \cdot E_{k_2} \right], \tag{20}$$

where the tensor product is easily calculated according to

$$\left[(\rho_K \otimes E_{k_1})_{k_2} \cdot E_{k_2} \right] = \sum_{Q,q_1,q_2} (-1)^{K-k_1} \sqrt{2k_2+1} \begin{pmatrix} K & k_1 & k_2 \\ Q & q_1 & -q_2 \end{pmatrix} E_{k_1 q_1} \rho_{KQ} E_{k_2 - q_2} \tag{21}$$

Here $E_{k_1 q_1}$ and $E_{k_2 - q_2}$ are polarization matrices with ranks k_1 and k_2, which correspond to the first and second photons, respectively. The proportionality constant C depends on the intensity of the probe light. The factor $S^{k_2}_{K k_1}$ depends on all quantum numbers of the initial, intermediate and final states involved in the two-photon process, but not on the projections of any tensors:

$$\begin{aligned} S^{k_2}_{K k_1}(j_i \gamma_i; j_f \gamma_f) = (-1)^{K+1} & \sqrt{(2K+1)(2k_1+1)} \\ & \times \sum_{j_e \gamma_e j'_e \gamma'_e} (-1)^{j_f + j'_e} \begin{Bmatrix} j_i & 1 & j_e \\ j_i & 1 & j'_e \\ K & k_1 & k_2 \end{Bmatrix} \begin{Bmatrix} j_e & j'_e & k_2 \\ 1 & 1 & j_f \end{Bmatrix} \\ & \times S(\gamma_i j_i, \gamma_e j_e, \gamma'_e j'_e, \gamma_f j_f). \end{aligned} \tag{22}$$

The quantum numbers j_i, j_e and j_f designate total angular momentum of initial, excited (intermediate or "virtual") and final states of the photofragment, respectively. The γ_i, γ_e, and γ_f are sets of all other fragment quantum numbers excluding projections. The presence of both j_e and j'_e as well as γ_e and γ'_e is a result of coherent sums over different intermediate excited states. The factor $S(\gamma_i j_i, \gamma_e j_e, \gamma'_e j'_e, \gamma_f j_f)$ contains reduced matrix elements and the energy denominator of second order time-dependent perturbation theory:

$$S(\gamma_i j_i, \gamma_e j_e, \gamma'_e j'_e, \gamma_f j_f) = \frac{\langle \gamma_f j_f \| d \| \gamma_e j_e \rangle \langle \gamma_f j_f \| d \| \gamma'_e j'_e \rangle^* \langle \gamma_e j_e \| d \| \gamma_i j_i \rangle \langle \gamma'_e j'_e \| d \| \gamma_i j_i \rangle^*}{(E_{ei} - h\nu + i\Gamma/2)(E_{e'i} - h\nu - i\Gamma/2)}. \tag{23}$$

Eqs (20)–(23) can be used for any polarization of the probe light and any experimental geometry. They are equivalent to those given by Kummel and coworkers [32] and by Docker [46], except that all projection information and laser polarization dependence have been factored out. The practical convenience of this modification lies in the complete separation between the scalar linestrength factor $S^{k_2}_{K k_1}$ and the tensor quantities in the photon-atom dot product. In this form, the qualitative dependence of the signal on laser polarization can be studied without reference to linestrengths.

We now write expressions for the 2+1 Resonance-Enhanced Multiphoton Ionization (2+1 REMPI) signal for three experimental geometries, corresponding to the linear probe laser

polarization along the axes **X**, **Y**, and **Z**. Using Eqs (20) and (21) with polarization tensor components

$$E_{00} = -\frac{1}{\sqrt{3}};\ E_{1q} = 0;\ E_{20} = \frac{2}{\sqrt{6}};\ E_{21} = 0;\ E_{22} = 0 \quad \text{for} \quad \mathbf{e} = e_Z$$
$$E_{00} = -\frac{1}{\sqrt{3}};\ E_{1q} = 0;\ E_{20} = -\frac{1}{\sqrt{6}};\ E_{21} = 0;\ E_{2\pm2} = \pm\frac{1}{2} \quad \text{for} \quad \mathbf{e} = e_X,\ e_Y, \tag{24}$$

we get

$$I_Z = C\left[P_0\rho_{00} + P_2\rho_{20} + P_4\rho_{40}\right] \tag{25}$$
$$I_{X,Y} = C\left[P_0\rho_{00} - \frac{P_2}{2}\left\{\rho_{20} \mp \sqrt{6}\mathrm{Re}[\rho_{22}]\right\} + \frac{P_4}{8}\left\{3\rho_{40} \mp 2\sqrt{10}\mathrm{Re}[\rho_{42}] + \sqrt{70}\mathrm{Re}[\rho_{44}]\right\}\right], \tag{26}$$

where

$$P_0 = \frac{1}{3}\left(S^0_{00} + 2S^2_{02}\right); \qquad P_2 = -\frac{\sqrt{2}}{3}\left(S^2_{20} + \frac{1}{\sqrt{5}}S^0_{22} + \frac{2}{\sqrt{7}}S^2_{22}\right); \qquad P_4 = \frac{2\sqrt{2}}{3\sqrt{7}}S^2_{42} \tag{27}$$

are the linestrength factors. The state multipoles ρ_{KQ} in Eqs (20), (21), (25), and (26) are not written as a function of recoil angles, but the expressions are general and valid both for the angle-dependent state multipoles $\rho_{KQ}(\theta,\phi)$ and for their angle-averaged values. The $-$ and $+$ of $\mp$ in Eq. (26) correspond to the **X** and **Y** probe polarizations, respectively. The multipole rank $K = 4$ in Eqs (25) and (26) corresponds to the maximum possible rank that can be detected using a two-photon detection technique. In order to detect odd-rank state multipoles, circularly polarized probe light should be used.

For $^2P^o_{3/2}$ ground state chlorine fragments, the rank $K = 4$ state multipoles do not exist [47], therefore we neglect them in our analysis. The fact that $\rho_{21}(\theta,\phi)$ and $\mathrm{Im}[\rho_{22}(\theta,\phi)]$ do not appear in Eqs (25) and (26) is simply a consequence of the experimental geometry. However, the fact that they do not contribute to the signal has no relation to whether they exist or not. As discussed in the previous section, multipoles that obey the relation $K \leq 2j_A$ will generally exist in the *laboratory* frame for any polarization of the dissociation light.

The spatial modulations in an ion image, Doppler profile, or TOFMS profile, which result from photofragment alignment, are often a relatively small fraction of the total signal. For this reason, it is useful to isolate the alignment contribution by taking linear combinations of the signal from different geometries, in such a way that the population term $\rho_{00}(\theta,\phi)$ cancels. Similarly, by combining measurements along all three Cartesian axes, the alignment terms can be eliminated. These expressions are

$$\frac{I_Z(\theta,\phi) - I_{X,Y}(\theta,\phi)}{\langle I_X\rangle + \langle I_Y\rangle + \langle I_Z\rangle} = \frac{\sqrt{2j_A+1}}{2}\frac{P_2}{P_0}\left[\rho_{20}(\theta,\phi) \mp \frac{\sqrt{6}}{3}\mathrm{Re}[\rho_{22}(\theta,\phi)]\right] \tag{28}$$
$$\frac{I_X(\theta,\phi) - I_Y(\theta,\phi)}{\langle I_X\rangle + \langle I_Y\rangle + \langle I_Z\rangle} = \frac{\sqrt{6(2j_A+1)}}{3}\frac{P_2}{P_0}\mathrm{Re}[\rho_{22}(\theta,\phi)] \tag{29}$$
$$\frac{I_X(\theta,\phi) + I_Y(\theta,\phi) + I_Z(\theta,\phi)}{\langle I_X\rangle + \langle I_Y\rangle + \langle I_Z\rangle} = \sqrt{j_A+1}\rho_{00}(\theta,\phi). \tag{30}$$

These equations have been normalized by $\langle I_X\rangle + \langle I_Y\rangle + \langle I_Z\rangle$, the sum of the total intensities along all three Cartesian axes. Each term such as $\langle I_X\rangle$ represents an integral over the coordinates of the corresponding spatially-resolved intensity $I_X(\theta,\phi)$. In practice, all three terms in the denominator can be obtained from spatially-resolved measurements in only two of the three geometries, because the two geometries with the probe polarization perpendicular to the photolysis polarization will have equal total intensities.

In practice, physical restrictions in the experimental apparatus may prevent measurements at certain geometries. For example, measuring both $I_X(\theta,\phi)$ and $I_Y(\theta,\phi)$ requires propagating the probe laser beam in two orthogonal directions, which may be impossible in some laboratories. This problem can be circumvented when the dissociation laser polarization lies parallel to the **Z** axis (Geometry I), since the image $M_X(\rho,\phi)$ [derived from $I_X(\theta,\phi)$] can be obtained by a simple 90° rotation of the image $M_Y(\rho,\phi)$. Nevertheless, in Sec. III of this work, we will consider only images corresponding to Eq. (28), which covers the most common experimental geometries.

For the spatially-unresolved intensities, Eqs (28) and (29) can be framed in terms of the familiar total alignment parameter [2,43]. For instance, if the dissociation light polarization is parallel to the **Z** axis (Geometry I), then only the $Q = 0$ multipole components contribute. The expressions are

$$\frac{\langle I_Z\rangle - \langle I_Y\rangle}{\langle I_Z\rangle + 2\langle I_Y\rangle} = \frac{\sqrt{2j_A+1}}{2}\frac{P_2}{P_0}\langle\rho_{20}\rangle = \frac{V(j_A)}{2\sqrt{5}}\frac{P_2}{P_0}\langle A_{20}\rangle \tag{31}$$

$$\langle I_X\rangle - \langle I_Y\rangle = 0, \tag{32}$$

where $\langle A_{20}\rangle$ is the space-fixed alignment parameter averaged over all recoil angles.

In order to calculate the linestrength factors P_K in Eqs (28)–(30), Eqs (22), (23), and (27) can be used directly. However, this usually requires numerical evaluation of the integrals in Eq. (23), which contain radial atomic wavefunctions. Fortunately, for certain values of the excited state quantum numbers, the linestrength factors P_K can be presented in an alternative form that avoids this difficulty. Using the symmetry properties of $3j$, $6j$, and $9j$ symbols and the summation rules for these symbols (see Appendix), one obtains

$$\begin{aligned} P_K = (-1)^{j_i+j_f}(2j_i+1)(2j_f+1)(2K+1)^{1/2}\sum_{T,R}(2T+1)(2R+1) \\ \times \begin{pmatrix} 1 & 1 & T \\ 0 & 0 & 0 \end{pmatrix}\begin{pmatrix} T & K & R \\ 0 & 0 & 0 \end{pmatrix}\begin{pmatrix} R & 1 & 1 \\ 0 & 0 & 0 \end{pmatrix}\begin{Bmatrix} j_i & j_i & K \\ T & R & j_f \end{Bmatrix} \\ \times \begin{Bmatrix} T & L_i & L_f \\ S & j_f & j_i \end{Bmatrix}\begin{Bmatrix} R & L_i & L_f \\ S & j_f & j_i \end{Bmatrix}\mathcal{L}(\bar\gamma_i L_i, \bar\gamma_f L_f), \end{aligned} \tag{33}$$

where

$$\mathcal{L}(\bar\gamma_i L_i, \bar\gamma_f L_f) = \sum_{\bar\gamma_e,\bar\gamma_e'}\sum_{L_e,L_e'}\begin{Bmatrix} T & L_i & L_f \\ L_e & 1 & 1 \end{Bmatrix}\begin{Bmatrix} R & L_i & L_f \\ L_e' & 1 & 1 \end{Bmatrix} S(\bar\gamma_i L_i, \bar\gamma_e L_e, \bar\gamma_e' L_e', \bar\gamma_f L_f,). \tag{34}$$

The factor $S(\bar\gamma_i L_i, \bar\gamma_e L_e, \bar\gamma_e' L_e', \bar\gamma_f L_f,)$ is defined in Eq. (23), L and S are fragment electron orbital and spin angular momenta, respectively. The symbol $\bar\gamma$ denotes the set of all other fragment quantum numbers other than j, L, and S.

Similar expressions for the linestrength factors were analyzed elsewhere (see for instance Refs [23,48,49]). By considering the symmetry properties of the $3j$ and $6j$ symbols [35], it can be seen from Eq. (33) that in general, R and T can take the values 0 or 2, but when $j_i \neq j_f$ or $L_i \neq L_f$, both R and T are restricted to the value 2. This allows a determination of the relative values of the linestrength factors P_K when $j_i \neq j_f$ or $L_i \neq L_f$, without computing the radial integrals. This important fact was first pointed out by Mo and Suzuki [23].

The analysis of Eq. (33) for $\mathrm{Cl}(^2P^o_{3/2})$ fragments is presented in Sec. IV B.

III. ALIGNMENT IMAGE BASIS FUNCTIONS

Eqs (28) and (29) in terms of θ and ϕ are readily converted to functions of two-dimensional image coordinates. It is apparent from Eqs (28) and (29) that the overall shape of the resulting difference images (or "alignment images") is independent of the quantitative value of the ratio P_2/P_0. For this reason, a great deal of information can be obtained without knowing the ratio P_2/P_0. Specifically, the symmetry of the excited states and whether coherent excitation has occurred is apparent from just the shapes of the difference images. This information corresponds to knowing relative values of the polarization anisotropy parameters. In contrast, to obtain quantitative information about nonadiabatic transition probabilities and optical excitation probabilities, one needs quantitative values of the alignment anisotropy parameters and thus also of the ratio P_2/P_0.

In most ion imaging studies to date, investigators sought to obtain recoil energy and angular distributions, using the inverse-Abel transform to directly invert their images to obtain the original three-dimensional ion spatial distribution [50]. However, this approach can only be used if the image is a projection of a cylindrically symmetric distribution, where the symmetry axis lies parallel to the two-dimensional surface. In general this condition is not met when crossed laser polarizations are employed, so the inverse-Abel transform cannot be used. Instead, we use the expression [51]

$$M(\rho,\phi) = 2\int_{\rho}^{\infty} \frac{f(\arcsin(\rho/r),\phi)g(r)}{\sqrt{1-\rho^2/r^2}}dr, \tag{35}$$

where $M(\rho,\phi)$ is an image or alignment image, ρ and ϕ are polar coordinates (ϕ is the same as in three dimensions), and r is the length of the photofragment radius vector. These variables are labeled clearly in Fig. 5. The function $f(\arcsin(\rho/r),\phi) \equiv f(\theta,\phi)$ describes the angular dependence of the intensity distribution and can be substituted with one of the REMPI intensity differences in Eq. (28). Eq. (35) assumes reflection symmetry of the function f in the X–Y plane. The function $g(r)$ describes the radial dependence of the three-dimensional distribution [52]. Unlike the Abel transform, Eq. (35) is not a true integral transform and cannot be inverted. Nevertheless, it may still be used for "forward-convolution" fitting of image data.

For monoenergetic chlorine atoms, $g(r) = \delta(r - r_0)$, where $r_0 = v_0\tau$, v_0 is the photofragment velocity, and τ is the flight time of the ions. For this special case, we can evaluate the integral in Eq. (35) analytically. Using Eq. (28) and Eq. (11) or (12) for f (in dissociation Geometries I or II, respectively) and substituting $\sin\theta = \rho/r_0$ gives the alignment images:

Geometry I: Dissociation light is linearly polarized along the **Z** axis:

$$\frac{M_Z(t,\phi)-M_Y(t,\phi)}{\langle M_Z\rangle+2\langle M_Y\rangle}=\frac{C'}{\sqrt{1-t^2}}\frac{P_2}{P_0}\Big\{[s_2-2\alpha_2+3\alpha_2 t^2][1-t^2(1+\sin^2\phi)]$$
$$-2\gamma_2 t^2(1-t^2)(1+\sin^2\phi)$$
$$-\frac{\eta_2}{4}t^2[3t^2+(2-t^2)\cos(2\phi)]\Big\}, \qquad (36)$$

Geometry II: Dissociation light is linearly polarized along the **Y** axis:

$$\frac{M_Z(t,\phi)-M_Y(t,\phi)}{\langle M_Y\rangle+2\langle M_Z\rangle}=\frac{C'}{\sqrt{1-t^2}}\frac{P_2}{P_0}\Big\{[s_2+\alpha_2(1-3t^2\sin^2\phi)][1-t^2(1+\sin^2\phi)]$$
$$+2\gamma_2 t^2\sin^2\phi[2-t^2(1+\sin^2\phi)]$$
$$+\frac{\eta_2}{2}[t^2(2-t^2)\cos(2\phi)+1-t^2+t^4(1-\frac{\sin^2(2\phi)}{4})]\Big\}, \qquad (37)$$

where $C'=\sqrt{5}V(j_A)/4\pi$ and $\langle M_Y\rangle$, $\langle M_Z\rangle$ are total image intensities for the two probe light polarizations. The variable t is the radial coordinate normalized to the maximum possible radius, *i.e.* $t=\rho/r_0$.

The alignment images described by Eqs (36) and (37) provide a powerful means for interpreting the alignment contribution to photofragment ion image data, since each of the four alignment mechanisms discussed in Sec. II A 1 is associated with a unique radial and angular dependence in the images. The alignment image "basis" functions shown in Fig. 6 are graphs of Eqs (36) and (37) for limiting values of the alignment anisotropy parameters. Linear combinations of these shapes can be used to simulate the contribution of rank 2 alignment to photofragment ion image data for dissociations that are initiated with linearly polarized light and that produce fragments with a single recoil velocity. These shapes are the final result of the theoretical approach discussed in this and the preceding sections.

Fig. 6(a) and (b) are the basis images for incoherent perpendicular and parallel excitation, respectively. Both geometries of the dissociation laser are shown. As discussed in Sec. II A 2, the alignment due to parallel and perpendicular transitions contains contributions from both s_2 and α_2. This is apparent from the definitions of the alignment anisotropy parameters in Eq. (8). Fig. 6(a) was obtained with s_2=$2\alpha_2$ and Fig. 6(b) with s_2=$-\alpha_2$. For both, η_2 and γ_2 were set to zero. The coherent contributions are shown in the third and fourth rows of the figure. Fig. 6(c) shows the basis images for coherent perpendicular excitation (η_2), while Fig. 6(d) shows the basis images for coherent excitation via both parallel and perpendicular transitions (γ_2).

For chlorine dissociation, which can produce only quadrupole (rank K=2) alignment, only the shapes in Fig. 6 are needed. For photofragments with angular momentum higher than 3/2, additional basis images are needed (although the rank 2 alignment is likely to be the major contribution). Rank $K=4$ can be treated by defining hexadecapole alignment anisotropy parameters α_4, s_4, η_4, and γ_4 from Eq (2) and then using Eqs (25), (26), and (2) to obtain the appropriate alignment image basis functions. For orientation (measurable with circularly polarized probe light), two additional sets of state multipoles with ranks $K=1$ (dipole orientation) and $K=3$ (octupole orientation) can be probed in a 2+1 REMPI

experiment. This case can be treated by using the general equations (20) and (2) in this paper and the set of orientation anisotropy parameters defined in Ref. [18].

IV. APPLICATION TO IMAGING OF CHLORINE PHOTODISSOCIATION

A. BACKGROUND ON CHLORINE DISSOCIATION

Our first application of the theoretical approach described in this paper is a study of orbital alignment in the ground state chlorine atoms produced by the dissociation of Cl_2 at 355 nm. The chlorine molecule is an excellent model system for the study of photodissociation dynamics, because its ultraviolet dissociation involves relatively few electronic states. Many basic features of the dissociation have already been well-characterized [53–57], including branching ratios and the angular distribution of photofragment density. These studies have paved the way for recent investigations, which reveal the more subtle phenomenon of photofragment polarization [19,21,58].

The lowest excited electronic states of the chlorine molecule involve promotion of an electron from a π_g antibonding orbital to a σ_u^+ antibonding orbital. The following molecular states originate from the $^2P^o_{3/2}$ states of isolated Cl atoms: one of 3_u symmetry, one of 2_u, one of 2_g, one of 1_g, two of 1_u, two of 0_u^-, and two of 0_g^+ (which includes the 0_g^+ state that correlates adiabatically with the ground $X^1\Sigma_{0_g^+}$ state of the molecule). A diagram showing adiabatic correlations between atomic and molecular states appears in Refs [55,56]. Potential curves have been calculated with *ab initio* [59] and asymptotic [60,61] methods. Several of these curves are shown in Fig. 4.

The $C^1\Pi_{1_u}$ and $A^3\Pi_{1_u}$ excited states, which correlate adiabatically with two ground state atoms, can be optically excited from the ground molecular state $X^1\Sigma_{0_g^+}$. It is well known that the dominant absorption at 355 nm results from excitation to the dissociative $C^1\Pi_{1_u}$ state of chlorine [53–57,59]. At this wavelength, the $A^3\Pi_{1_u}$ state contributes negligibly to absorption [62]. A shoulder in the absorption spectrum at longer wavelength results primarily from absorption to the $B^3\Pi_{0_u^+}$ state, which correlates to one ground state and one spin-orbit excited state ($^2P^o_{1/2}$) atom.

B. ANALYSIS OF LINESTRENGTH FACTORS

In order to quantitatively determine the degree of photofragment alignment, we must know the alignment sensitivity of the two-photon states used in our measurements. Here, we use Eq. (33) to analyze the linestrength factors P_K for detection of aligned ground state $Cl(^2P^o_{3/2})$ fragments.

a. $^2P^o_{3/2} \rightarrow\!\!\rightarrow {}^2S^o_{1/2}$ *detection.* The relevant quantum numbers are $j_i = \frac{3}{2}; L_i = 1; j_f = \frac{1}{2}; L_f = 0$. As discussed in Sec. II B, the indices T and R in Eq. (33) are restricted to the value $T = R = 2$. Substituting these values into Eq. (33), we see that the function $\mathcal{L}(\bar{\gamma}_i L_i, \bar{\gamma}_f L_f)$ in Eq. (34) is equal to zero due to the symmetry properties of the $6j$ symbols [35]. This means that the two-photon transition $^2P^o_{3/2} \rightarrow\!\!\rightarrow {}^2S^o_{1/2}$ is forbidden and can occur only due to an admixture of $^2P^o_{1/2}$ atomic states with the $^2S^o_{1/2}$ state, from spin-orbit interaction in

the Cl atom. Thus in order to obtain the linestrength factors for this transition, one must use $L_f = 1$ instead of $L_f = 0$. From Eq. (33) we get

$$\frac{P_2}{P_0} = -1. \tag{38}$$

b. $^2P^o_{3/2} \rightarrow\rightarrow {}^2D^o_j$ *detection.* The quantum numbers to be used in Eq. (33) are $j_i = \frac{3}{2}; L_i = 1; j_f = \frac{3}{2}, \frac{5}{2}; L_f = 2$. Again, the indices T and R both equal 2. For $j_f = 3/2$, the $6j$ symbol in Eq. (33) containing K=2 is equal to zero. This means that the pure $^2P^o_{3/2} \rightarrow\rightarrow {}^2D^o_{3/2}$ transition is allowed but not sensitive to ground state alignment. Our previous observation of alignment signal for this transition [21] implies the presence of a spin-orbit-mediated admixture of $^2P^o_{3/2}$ character into the $^2D^o_{3/2}$ state, since a $^2P^o_{3/2} \rightarrow\rightarrow {}^2P^o_{3/2}$ transition would be alignment-sensitive according to Eq. (33).

To simplify the quantitative analysis in this paper, we used the transition $^2P^o_{3/2} \rightarrow\rightarrow {}^2D^o_{5/2}$, which has a simple expression for the linestrength factors ratio. By using $j_f = 5/2$ and substituting into Eq. (33), we get

$$\frac{P_2}{P_0} = \frac{5}{7}. \tag{39}$$

Note that possible admixture of $^2F^o_{5/2}$ atomic states with the $^2D^o_{5/2}$ atomic state does not change this result, because according to Eq. (33), it does not depend on the quantum number L_f.

C. EXPERIMENT

1. Experimental Setup

In general, in order to study the polarization angular distribution, one must simultaneously measure recoil velocity vectors and the correlated angular momentum polarization. In our study, we have used two-dimensional photofragment ion imaging [63] and 2+1 REMPI for this purpose.

Fig. 3 shows a schematic diagram of our experimental apparatus. This standard ion imaging apparatus consists of a time-of-flight mass spectrometer and a position-sensitive detector. A pulsed (10 Hz) solenoid valve produces a supersonic expansion of chlorine molecules (10% seeded in Ar). The beam is skimmed and enters the interaction region of the mass spectrometer, where it crosses two counter-propagating laser beams at 90°.

The initial laser pulse (355 nm) dissociates a small fraction of the chlorine molecules. After a delay of 10–20 ns, the nascent atomic photofragments are state-selectively ionized by a second pulse (236.284 nm or 234.640 nm [64]) via a 2+1 REMPI transition [$\mathrm{Cl}(3p\,^2P^o_{3/2}) \rightarrow\rightarrow \mathrm{Cl}(4p\ ^2S^o_{1/2}$ or $^2D^o_{5/2}) \rightarrow \mathrm{Cl}^+$]. During image acquisition, the wavelength of the probe laser light is repeatedly scanned over the Doppler profile of the line to sample the entire velocity distribution. The polarizations of the two lasers were >99% linear, as measured with a Glann-Taylor prism polarizer. Each polarization could be rotated with an appropriate half-wave plate.

The photofragments are ionized between repeller and attractor plates, which are set at voltages corresponding to velocity-map imaging conditions [65]. The ion packet travels through a field free flight tube and strikes dual microchannel plates, which are gated at the flight time of the chlorine atomic ions. Electrons emerging from the back of the microchannel plate strike a phosphor screen to produce images of the spatial distribution of the ionized photofragments.

Images were collected with a cooled CCD camera and signal-averaged for 15 minutes at each of four geometries of the dissociation and probe laser polarizations. To further improve the signal-to-noise ratio, we used an image processor to combine the raw data images with their horizontal and vertical reflections. A photomultiplier tube behind the phosphor screen was used to measure the total image intensity. This was used to obtain mass spectra, to optimize signal, and to measure the total alignment in the laboratory frame.

2. Total Alignment Measurement

We determined the total alignment $\langle A_{20} \rangle$ in the laboratory frame by measuring total signal intensities for parallel and perpendicular relative polarizations of the dissociation and probe lasers. Because of drifts in experimental conditions, including the molecular beam and laser intensities, we improved the measurement statistics by alternately changing the polarization of one of the lasers every thirty seconds, averaging for a total of 30 minutes at each position. This gives the ratio of intensities for parallel and perpendicular relative orientations of the dissociation and probe laser polarizations, $I_{\|}/I_{\perp} = 1.04(4)$ for the $^2S^o_{1/2}$ state and 0.99(10) for the $^2D^o_{5/2}$ state.

Using these values in Eq. (31), with $V(3/2) = 5\sqrt{5}/4$, $P_2/P_0 = -1$ or 5/7 for the $^2S^o_{1/2}$ and $^2D^o_{5/2}$ state, respectively, and including an additional factor of 3.7 to account for the effect of hyperfine depolarization [67], gives a total alignment $\langle A_{20} \rangle = -0.08(8)$ from the $^2S^o_{1/2}$ state and $-0.01(15)$ from the $^2D^o_{5/2}$ state. These values are the same within their error bars.

3. Cl Photofragment Alignment Two-Photon Detection via the $^2S^o_{1/2}$ and $^2D^o_{5/2}$ Excited States

We have measured ion images using the four different combinations of laser polarizations discussed in Sec. III, *i.e.* the dissociation and probe laser polarizations both parallel and perpendicular to the **Z** axis (ion flight axis). The **Z** and **Y** polarizations of the dissociation laser are identified as Geometries I and II, respectively. For all measurements, the lasers were counterpropagating along the **X** axis. Ion image data for chlorine dissociation in these four geometries are shown in Fig. 7, for both $^2S^o_{1/2}$ and $^2D^o_{5/2}$ probe states.

The shape of the data images is predominantly influenced by the population distribution $\rho_{00}(\theta, \phi)$, described by the β_0 parameter, which is close to the limiting value of -1 for this perpendicular transition. There is a small difference between images measured with different probe laser polarizations (compare first and third with second and fourth rows, respectively). This difference is a consequence of angular momentum alignment.

From the raw data images in Fig. 7, we wish to obtain alignment images as prescribed by Eqs (36) and (37). In an ideal experiment, where no intensity-altering conditions change between the **Z** and **Y** measurements, it would be possible to directly subtract the measured images, $M_Z(t,\phi)$ and $M_Y(t,\phi)$. Because of slow drifts in experimental conditions, this is nearly impossible in practice, unless one carries out a shot-to-shot rotation of the probe laser polarization and collects two separate images in parallel. In the next section, we discuss two alternatives to carrying out this direct image subtraction.

Fig. 8 (first and third rows) shows the alignment images corresponding to the left side of Eqs (36) and (37), obtained from the data of Fig. 7.

4. Determination of Alignment Anisotropy Parameters

A measured alignment image can be simulated as a linear combination of the four basis images shown in Fig. 6, each of which corresponds to a specific alignment mechanism. Since alignment images correspond exactly to the left sides of Eqs (11) and (12), and all other values on the right side of this equation are known, a fit to the experimental alignment images will give properly normalized values of the alignment anisotropy parameters.

To get the correct alignment image on the left side of Eqs (11) and (12), it is crucial that the measured images, which would equal $M_Z(t,\phi)$ and $M_Y(t,\phi)$ in the ideal case, have the proper relative normalizations. As discussed in the previous section, it is usually not appropriate to directly subtract the raw data images, because the relative intensities may be incorrect due to experimental drift. We suggest two alternative approaches which may be used to do a properly weighted subtraction of the data images.

The first option is to use the measured ratio of total intensities $I_{\|}/I_{\perp}$ (Sec. IV C 2) to properly weight the measured images. To do this, both images are normalized to an integrated value of one, giving $M_Z^{norm}(t,\phi)$ and $M_Y^{norm}(t,\phi)$, respectively. Then, the alignment images corresponding to the left side of Eqs (36) and (37) become:

$$\text{Geometry I:} \qquad \frac{(I_{\|}/I_{\perp})M_Z^{norm}(t,\phi) - M_Y^{norm}(t,\phi)}{I_{\|}/I_{\perp}+2}, \tag{40}$$

$$\text{Geometry II:} \qquad \frac{M_Z^{norm}(t,\phi) - (I_{\|}/I_{\perp})M_Y^{norm}(t,\phi)}{I_{\|}/I_{\perp}+2}, \tag{41}$$

respectively. This approach is preferable when the uncertainty in the measured value of $I_{\|}/I_{\perp}$ is smaller than the average uncertainty in the pixel-position-dependent image intensities (as a fraction of the *difference* image intensities), which results from experimental spatial distortions in the images.

A second option, which we will use, is more appropriate when the uncertainty in $I_{\|}/I_{\perp}$ is large. This approach is to start with a trial value of $I_{\|}/I_{\perp}$, calculate the alignment images according to Eqs (40) and (41), and then iteratively improve $I_{\|}/I_{\perp}$ by repeated fitting and recalculation of the alignment images until a self-consistent result is obtained. By doing this, we are recognizing that $I_{\|}/I_{\perp}$ is proportional to $\langle A_{20}\rangle = -2(\alpha_2+\gamma_2+\eta_2)$ [Eq. (10)], so in effect, the unknowns which we wish to obtain by fitting appear on both sides of Eqs (36) and (37).

For either of these two approaches, one fits the left side of Eqs (36) and (37) by optimizing the alignment parameters on the right side (or equivalently, the relative weightings of basis functions shown in Fig. 6). We used the Singular Value Decomposition (SVD) technique for this purpose (see *e.g.* Ref. [68]). The basis images were first convoluted with a Gaussian to mimic the experimental spatial resolution, which is evident as a slight blurring of the experimental images. Since several of the unconvoluted basis images have sharp features which go to infinity at $t = 1$, care was taken that grid size effects did not influence the parameters obtained from the fit.

The alignment parameters obtained by fitting the data for both probe states are shown in Table I. These fits were obtained using the iterative procedure described above. Even extreme initial trial values of $I_{\parallel}/I_{\perp}$ converged quickly to the same set of alignment anistropy parameters and final value of $I_{\parallel}/I_{\perp}$. The average of the results for both probe states (fourth column) is the quantitative final result of our fitting procedure. The size of the error margins represents the standard deviation associated with averaging four (nominally) equivalent image quadrants in multiple data sets for both $^2S^o_{1/2}$ and $^2D^o_{5/2}$ probe states. This uncertainty reflects the spatial inhomogeneity of the images and the modest effects of changes in experimental conditions during the course of the investigation. From the alignment anisotropy parameters in Table I, we can also obtain a value for $\langle A_{20} \rangle$, using Eq. (10). This value compares favorably with the value obtained from the independent measurement of $I_{\parallel}/I_{\perp}$.

The simulated images corresponding to the alignment anistropy parameters in Table I are shown in the second and fourth rows of Fig. 8. The features of the measured images are very well represented in these fits. The fits include substantial contributions from basis images (a) and (c) of Fig. 6, which correspond to incoherent and coherent perpendicular excitation, respectively.

V. DISCUSSION

It has been firmly established through measurements of the angular distribution of photofragment density (velocity anisotropy), that 355 nm excitation in chlorine occurs primarily through a perpendicular transition [53–57,59]. In this work, we have provided experimental evidence that the excitation symmetry also has a profound influence on the alignment angular distribution. This is apparent from the large contribution of the alignment image basis functions in the row (a) of Fig. 6. Our analysis also identifies something quite new for chlorine—a coherent contribution to the photoexcitation. Coherence effects have been seen before in total alignment measurements (*e.g.* for the calcium dimer [12,39]), but these measurements are not capable of fully separating coherent and incoherent contributions to the alignment. Whereas total alignment measurements give the sum $\alpha_2 + \gamma_2 + \eta_2$, **v**–**j** correlation measurements make it possible to determine each alignment anisotropy parameter individually.

At first glance, the contribution to photofragment alignment from coherent perpendicular excitation may seem unsurprising. The $C^1\Pi_{1_u}$ state of chlorine, which is believed to be the primary absorber, contains a degenerate pair of $|\Omega|$=1 states. One might conclude therefore, that coherent excitation of these states followed by adiabatic dissociation, is all that is required to explain the observed coherence effect. In fact, the coherent contribution

to alignment also requires the occurence of nonadiabatic transitions during separation of the two chlorine atoms. In this section, we take a closer look at the physics of photofragment alignment, which is relevant to understanding this fact. We start by considering a purely adiabatic dissociation, which is sufficient to qualitatively explain the incoherent contribution to alignment.

A. Adiabatic Dissociation

The two lowest molecular states of 1_u symmetry can be expanded in the asymptotic region over the atomic basis $|j_1\Omega_1, j_2\Omega_2\rangle$ as

$$|1_u\rangle_a \overset{R\to\infty}{\longrightarrow} \frac{1}{\sqrt{2}}\left(|\tfrac{3}{2}\tfrac{3}{2}, \tfrac{3}{2} -\tfrac{1}{2}\rangle + |\tfrac{3}{2} -\tfrac{1}{2}, \tfrac{3}{2}\tfrac{3}{2}\rangle\right) \tag{42}$$

$$|1_u\rangle_c \overset{R\to\infty}{\longrightarrow} |\tfrac{3}{2}\tfrac{1}{2}, \tfrac{3}{2}\tfrac{1}{2}\rangle \tag{43}$$

and have the following long-range Coulomb interaction energies [61]:

$$E^a_{int} \approx -\frac{0.182}{R^5} - \frac{0.521}{R^6} \tag{44}$$

$$E^c_{int} \approx \frac{0.344}{R^5} - \frac{0.507}{R^6}. \tag{45}$$

The states $|1_u\rangle_a$ and $|1_u\rangle_c$ correlate adiabatically with the states $A^3\Pi_{1_u}$ and $C^1\Pi_{1_u}$ of Cl_2, respectively (see Fig. 4). The T matrix elements in Eq. (5) are obtained from Eqs (42) and (43):

$$\begin{aligned} T^{A1_u}_{\frac{3}{2}\frac{3}{2}\,\frac{3}{2}-\frac{1}{2}} &= \frac{1}{\sqrt{2}} \\ T^{A1_u}_{\frac{3}{2}-\frac{1}{2}\,\frac{3}{2}\frac{3}{2}} &= \frac{1}{\sqrt{2}} \\ T^{C1_u}_{\frac{3}{2}\frac{1}{2}\,\frac{3}{2}\frac{1}{2}} &= 1. \end{aligned} \tag{46}$$

Equivalent expressions apply for T matrix elements with opposite signs of all projection quantum numbers, *i.e.*, $T^{n1}_{j_A\Omega_A\, j_B\Omega_B} = T^{n-1}_{j_A-\Omega_A\, j_B-\Omega_B}$ (with $n = a, c$), which agrees with the symmetry relations of the dynamical functions [Eq. (4)]. All other elements of the T matrix are equal to zero.

We can now calculate the photofragment alignment. For an adiabatic dissociation, we have $N^{n_e\Omega\; n'_e\Omega'}_{n\Omega\; n'\Omega'}$ equal to 1 for $n_e{=}n$ and equal to zero for $n_e{\neq}n$. Using Eqs (3) and (5) for the dynamical functions, we obtain for $K = 0, 2$:

Dissociation via the $A^3\Pi_{1_u}$ state

$$f_0(1,1) = \frac{d^2_{A_1}}{2}; \quad f_2(1,1) = 0; \quad f_2(1,-1) = 0 \tag{47}$$

Dissociation via the $C^1\Pi_{1_u}$ state

$$f_0(1,1) = \frac{d_{C_1}^2}{2}; \quad f_2(1,1) = -\frac{d_{C_1}^2}{2\sqrt{5}}; \quad f_2(1,-1) = 0 \tag{48}$$

where $d_{A_1}=\langle\Phi_0(R)|\Phi_1(R)\rangle\langle 0|d_1|A,1\rangle$, and a similar expression applies for d_{C_1}. These results show that photodissociation via the $A^3\Pi_{1_u}$ excited molecular state does not produce photofragment alignment. In contrast, photodissociation via the $C^1\Pi_{1_u}$ excited molecular state leads to photofragment alignment due to an incoherent dissociation mechanism, although no alignment is produced by a coherent mechanism. Note that these results are a direct consequence of the symmetry of the long-range molecular wavefunctions that were obtained under the assumption of a purely adiabatic dissociation.

The degree of photofragment alignment that can be obtained through photodissociation via the $C^1\Pi_{1_u}$ excited state is described by the alignment anisotropy parameters α_2, s_2, and η_2 [Eq. (8)], which have the values

$$\alpha_2 = \frac{s_2}{2} = -\frac{2}{25}; \qquad \eta_2 = 0. \tag{49}$$

Converting to molecular frame alignment parameters using Eqs (7) and (18), one obtains

$$A_{20}^{mol} = 10\alpha_2 = -\frac{4}{5}; \qquad A_{22}^{mol} = 0. \tag{50}$$

This value of the molecular frame alignment parameter A_{20}^{mol} is equal to its most negative possible value (see, for instance Ref. [2]), showing that the $\Omega_A = \pm 1/2$ fragment magnetic sublevels are equally populated while the $\Omega_A = \pm 3/2$ magnetic sublevels are empty. Thus both fragments' angular momenta $j = 3/2$ are mainly perpendicular to the molecular axis.

Although the ratio of s_2 to α_2 obtained from our measurements is similar to that in Eq. (49), the individual values are considerably smaller. The adiabatic analysis also predicts a value of zero for η_2, at odds with our measurements. In order to explain the measured alignment, one must consider the role of nonadiabatic interactions.

B. Dissociation with Nonadiabatic Interactions

We consider homogeneous nonadiabatic transitions between the nascent $C^1\Pi_{1_u}$ state and the $A^3\Pi_{1_u}$ state of chlorine. Since there are no avoided crossings involving these two states, nonadiabatic transitions can occur only at relatively long range, where the energy gap between the $A^3\Pi_{1_u}$ and $C^1\Pi_{1_u}$ states becomes comparable in magnitude to the matrix elements which describe their nonadiabatic coupling. Nonadiabatic interactions are represented in the theory by factors $N_{n\Omega\ n'\Omega'}^{n_e\Omega\ n'_e\Omega'} \equiv \langle n_e,\Omega|N|n,\Omega\rangle\langle n'_e,\Omega'|N|n',\Omega'\rangle^*$, with $n_e \neq n$ and $n'_e \neq n'$ [Eq. (5)]. The operator N is the nonadiabatic part of the scattering matrix in the axial recoil approximation. The probability w of the nonadiabatic transition is defined as $w = |\langle C,1|N|A,1\rangle|^2 = |\langle C,-1|N|A,-1\rangle|^2$.

For incoherent excitation of a $|C,\Omega\rangle$ substate followed by dissociation, the molecule can remain in the same substate, transfer to the $|A,\Omega\rangle$ substate, or appear in a coherent superposition of both (see Figs 9(a), (b), and (c), respectively). According to Eqs (3) and (5), only the first of these dissociation channels leads to a nonzero dynamical function $f_2(1,1)$,

resulting in a photofragment alignment component A_{20}^{mol} as discussed in the previous section. The probability of this channel is $|\langle C,1|N|C,1\rangle|^2 = (1-w)$.

For coherent excitation of the $|C,\Omega{=}\pm1\rangle$ substates, the molecule can end up in the same substates, a coherent superposition of the $|A,\Omega{=}\pm1\rangle$ substates, or a coherent superposition of $|C,\Omega{=}\pm1\rangle$ and $|A,\Omega{=}\mp1\rangle$. These possibilities are shown in Figs 9(d), (e), and (f), respectively. The first two of these three dissociation channels result in values of zero for the alignment dynamical functions $f_2(q,q')$. However, the third channel results in a nonzero value for the dynamical function $f_2(1,-1)$, which is related to the photofragment alignment component A_{22}^{mol}. This component is proportional to the "coherent" off-diagonal nonadiabatic transition matrix element $w_{\rm coh} = {\rm Re}[\langle C,1|N|A,1\rangle\langle C,-1|N|C,-1\rangle^*] = {\rm Re}[\langle C,1|N|A,1\rangle\langle C,1|N|C,1\rangle^*]$, which can be either positive or negative depending on the details of the nonadiabatic interaction.

Using Eqs (3), (5), and (46), the dynamical functions are

$$f_0(1,1) = \frac{d_{C_1}^2}{2}; \quad f_2(1,1) = -\frac{(1-w)d_{C_1}^2}{2\sqrt{5}}; \quad f_2(1,-1) = -\frac{w_{\rm coh}d_{C_1}^2}{\sqrt{5}}. \tag{51}$$

The above expression for the "coherent" dynamical function $f_2(1,-1)$ makes use of the fact that $d_{C_1} = -d_{C_{-1}}$, which can be obtained from the symmetry properties of the wavefunctions $|1_u\rangle_c$ [Eq. (43)] and the cyclic components d_q of the electric dipole moment operator. The anisotropy parameters α_2 and η_2, which describe the contribution to photofragment alignment resulting from incoherent and coherent excitation, respectively, can be obtained from Eqs (8) and (51):

$$\alpha_2 = \frac{s_2}{2} = -\frac{2(1-w)}{25}; \qquad \eta_2 = -\frac{4\sqrt{6}w_{\rm coh}}{25}. \tag{52}$$

The corresponding molecular frame alignment parameters [Eqs (7) and (18)] are

$$A_{20}^{mol} = -\frac{4(1-w)}{5}; \qquad A_{22}^{mol} = \frac{4w_{\rm coh}}{5}. \tag{53}$$

Comparing the above expressions for the alignment anisotropy parameters to the values obtained in the experiment, we can draw conclusions about the mechanisms responsible the Cl photofragment alignment.

The first important contribution to the experimental signals is the incoherent excitation mechanism. Eqs (52) and (53) show that the photofragment alignment produced by incoherent excitation of the molecular $C^1\Pi_{1_u}$ state is negative and equal to approximately half of its most negative possible value. This deviation from the extremum is a consequence of the homogeneous nonadiabatic transition from the $C^1\Pi_{1_u}$ state of the chlorine molecule to the $A^3\Pi_{1_u}$ state. Using Eq. (52) we can calculate the probability of this nonadiabatic transition to be $w = 0.60(4)$.

The second important contribution to the experimental signals is the coherent excitation mechanism. The coherence is initiated by optical excitation to components $\Omega = \pm1$ of the $C^1\Pi_{1_u}$ state, however a nonadiabatic transition later in the dissociative process is required for the coherence to have observable consequences. This nonadiabatic transition produces a system that dissociates along two indistinguishable pathways (the $C^1\Pi_{1_u}$ and $A^3\Pi_{1_u}$ asymptotic

curves), which can interfere to produce modulations—interference fringes—in the alignment angular distribution. According to Table I and Eqs (52) and (53), the contribution to molecular frame alignment from coherent excitation is negative and proportional to the "coherent" nonadiabatic probability w_{coh}, calculated to be $w_{coh} = -0.19(5)$. The negative sign of w_{coh} may result from the phase difference between the wavefunctions of the $C^1\Pi_{1_u}$ and $A^3\Pi_{1_u}$ molecular states. This phase difference is produced both by the nonadiabatic transition itself and during the subsequent evolution of the molecular system along the $C^1\Pi_{1_u}$ and $A^3\Pi_{1_u}$ asymptotic curves [69]. A comprehensive description of chlorine dissociation that includes this phase difference is the subject of ongoing investigation.

VI. CONCLUSION

We have developed a technique for extracting information on dissociation dynamics from measurements of the recoil angular distribution of atomic photofragment alignment. By applying this method to experimental data, one obtains a set of alignment anisotropy parameters, which describe excited state symmetries, coherence effects, and nonadiabatic transitions. This analysis emphasizes the application to ion imaging experiments, however, it can be readily adapted to other common experimental techniques that combine two-photon excitation with measurement of the photofragment spatial or velocity distribution.

To demonstrate the power of this analysis technique, we have undertaken an ion imaging study of polarized atoms, which are produced by molecular chlorine photodissociation. Analyzing the experimental results with the methods described in this paper leads to a much deeper understanding of this already well known system. We have shown that the atomic alignment is a consequence of both incoherent and coherent perpendicular excitation to the $C^1\Pi_{1_u}$ state of chlorine. In order to explain the coherent contribution to alignment and the non-maximal value of the incoherent contribution, we have shown that a nonadiabatic transition to the $A^3\Pi_{1_u}$ state must have occurred in the asymptotic region of the chlorine potential energy curves.

ACKNOWLEDGMENTS

The authors thank Dr. T.P. Rakitzis and Dr. R.N. Zare for helpful discussions. This work was supported by the Director, Office of Energy Research, Office of Basic Energy Sciences, Chemical Sciences Division of the U.S. Department of Energy under Contract No. DE-AC03-76SF00098, and by a Cooperative Grant from the Civilian Research and Development Foundation, CRDF Award No. RP1-223.

APPENDIX: TRANSFORMATION OF THE EXPRESSION FOR THE LINESTRENGTH FACTORS P_K

The expression for the linestrength factors P_K [Eqs (22), (23), and (27)] can be transformed as follows. Having in mind that the atomic dipole moment operators in Eq. (23) do not depend on the electron spin S, Eq. (23) can be rewritten as follows [35]

$$S(j_i\gamma_i, j_e\gamma_e, j'_e\gamma'_e, j_f\gamma_f) = (-1)^{j_e+j'_e+L_e+L'_e+2j_i}(2J_i+1)(2J_e+1)(2J'_e+1)(2J_f+1)$$
$$\times \begin{Bmatrix} L_e & S & j_e \\ j_f & 1 & L_f \end{Bmatrix} \begin{Bmatrix} L_e & S & j_e \\ j_i & 1 & L_i \end{Bmatrix} \begin{Bmatrix} L'_e & S & j'_e \\ j_i & 1 & L_i \end{Bmatrix} \begin{Bmatrix} L'_e & S & j'_e \\ j_f & 1 & L_f \end{Bmatrix} \quad \text{(A1)}$$
$$\times \frac{\langle L_f \| d \| L_e \rangle \langle L_f \| d \| L'_e \rangle^* \langle L_e \| d \| L_i \rangle \langle L'_e \| d \| L_i \rangle^*}{(E_{ei} - h\nu + i\Gamma/2)(E_{e'i} - h\nu - i\Gamma/2)}.$$

Using the definition of the light polarization matrices $E_{kq}(\mathbf{e})$ [2] for the light polarization vector $\mathbf{e}$ parallel to the laboratory $\mathbf{Z}$ axis, and using the summation rule (7) from Chapter 12.1 of Ref. [35], the tensor product [Eq. (21)] can be rewritten as

$$[(\rho_K \otimes E_{k_1})_{k_2} \cdot E_{k_2}] = (-1)^{K+k_2}\rho_{K0}\delta_{q,0}\delta_{q',0}(2k_1+1)^{1/2}(2k_2+1) \quad \text{(A2)}$$
$$\times \sum_{q_1,q_2} \begin{pmatrix} 1 & 1 & k_1 \\ q & -q & q_1 \end{pmatrix} \begin{pmatrix} k_1 & K & k_2 \\ -q_2 & 0 & -q_2 \end{pmatrix} \begin{pmatrix} k_2 & 1 & 1 \\ q_2 & q' & -q' \end{pmatrix}$$
$$= (-1)^{K+k_2}\rho_{K0}\delta_{q,0}\delta_{q',0}(2k_1+1)^{1/2}(2k_2+1)$$
$$\times \sum_{T,t}\sum_{R,r}(2T+1)(2R+1) \begin{pmatrix} 1 & 1 & T \\ q & q' & t \end{pmatrix}$$
$$\times \begin{pmatrix} T & K & R \\ -t & 0 & -r \end{pmatrix} \begin{pmatrix} R & 1 & 1 \\ r & -q & -q' \end{pmatrix} \begin{Bmatrix} 1 & 1 & k_1 \\ 1 & 1 & k_2 \\ T & R & K \end{Bmatrix}$$

Carrying out the summation over indices k_1 and k_2 in Eq. (20) using the summation rules (12) and (27) from Chapter 12.2 of Ref. [35], yields

$$\sum_{k_1,k_2}(-1)^{k_2}(2k_1+1)(2k_2+1) \begin{Bmatrix} j_i & 1 & j_e \\ j_i & 1 & j'_e \\ K & k_1 & k_2 \end{Bmatrix} \begin{Bmatrix} 1 & 1 & k_1 \\ 1 & 1 & k_2 \\ T & R & K \end{Bmatrix} \begin{Bmatrix} j_e & j'_e & k_2 \\ 1 & 1 & j_f \end{Bmatrix} \quad \text{(A3)}$$
$$= (-)^{T+K+j'_e-j_i+1} \begin{Bmatrix} j_f & 1 & j_e \\ 1 & j_i & T \end{Bmatrix} \begin{Bmatrix} j_f & 1 & j'_e \\ 1 & j_i & R \end{Bmatrix} \begin{Bmatrix} j_i & j_i & K \\ T & R & j_f \end{Bmatrix}$$

Finally, the summation over j_e and j'_e in Eq. (22) is done by twice applying the summation rule (18) from Chapter 12.2 of Ref. [35]. This yields Eq. (25), with the linestrength factors P_K given in Eqs (33) and (34). Note that the summation over j_e and j'_e is done with only minimal loss of accuracy of Eq. (22), because for the Cl atom (and many other atoms), the denominator in Eq. (23) depends only slightly on the spin-orbit splittings between the energy levels of $|\bar{\gamma}_e S L_e j_e\rangle$ and $|\bar{\gamma}_e S L_e j'_e\rangle$.

REFERENCES

[1] K. Blum, *Density Matrix Theory and Applications*, Plenum, New York, 2nd edition, 1996.

[2] R.N. Zare, *Angular Momentum*, World Scientific, New York, 1988.

[3] A.C.G. Mitchell, Z. Phys. **49**, 228 (1928).

[4] R.J. Van Brunt and R.N. Zare, J. Chem. Phys. **48**, 4304 (1968).

[5] O.S. Vasyutinskii, Sov. Phys. JETP Lett. **31**, 428 (1980).

[6] O.S. Vasyutinskii, Sov. Phys. JETP **54**, 855 (1981).

[7] E.W. Rothe, U. Krause, and R. Duren, Chem. Phys. Lett. **72**, 100 (1980).

[8] Y. B. Band, K. F. Freed, and D. J. Kouri, Chem. Phys. Lett. **79**, 233 (1981).

[9] Y.B. Band and K.F. Freed, Chem. Phys. Lett. **79**, 238 (1981).

[10] Y.B. Band, K.F. Freed, and S.J. Singer, J. Chem. Phys. **72**, 6060 (1983).

[11] Y.B. Band, K.F. Freed, and S.J. Singer, J. Chem. Phys. **84**, 3762 (1986).

[12] J. Vigué, J.A. Beswick, and M. Broyer, J. Physique **44**, 1225 (1983).

[13] M. Glass-Maujean and J.A. Beswick, Phys. Rev. A **36**, 1170 (1987).

[14] M. Glass-Maujean and J.A. Beswick, Phys. Rev. A **38**, 5660 (1988).

[15] D.V. Kupriayanov and O.S. Vasyutinskii, Chem. Phys. **171**, 25 (1993).

[16] J.A. Beswick and O.S. Vasyutinskii, Comments At. Mol. Phys. (1998), in press.

[17] P.D. Kleiber, J.-X. Wang, K.M. Sando, V. Zafiropulos, and W.C. Stwalley, J. Chem. Phys. **95**, 4168 (1991).

[18] B.V. Picheyev, A.G. Smolin, and O.S. Vasyutinskii, J. Phys. Chem. **101**, 7614 (1997).

[19] Y. Wang, H.P. Loock, J. Cao, and C.X.W. Qian, J. Chem. Phys. **102**, 808 (1995).

[20] T.P. Rakitzis, S.A. Kandel, and R.N. Zare, J. Chem. Phys. **108**, 8291 (1998).

[21] A.S. Bracker, E.R. Wouters, A.G. Suits, Y.T. Lee, and O.S. Vasyutinskii, Phys. Rev. Lett. **80**, 1626 (1998). Please note the typographical errors: the ratio of anisotropy parameters that was set equal to -1.5 is s_2/η_2, not α_2/η_2; also a factor 3 was omitted in its Eq. (3b) (*cf.* Eq. (36) in this paper). This affects Geometry I, image (c) in Fig. 6.

[22] T. Suzuki, H. Katayanagi, Y. Mo, and K. Tonokura, Chem. Phys. Lett. **256**, 90 (1996).

[23] Y. Mo, H. Katayanagi, M.C. Heaven, and T. Suzuki, Phys. Rev. Lett. **77**, 830 (1996).

[24] A.T.J.B. Eppink, D.H. Parker, M.H.M. Janssen, B. Buijsse, and W.J. van der Zande, J. Chem. Phys. **108**, 1305 (1998).

[25] P.L. Houston, J. Phys. Chem. **91**, 5388 (1987).

[26] J.P. Simons, J. Phys. Chem. **91**, 5378 (1987).

[27] R.N. Dixon, J. Chem. Phys. **85**, 1866 (1986).

[28] G.E. Hall, N. Sivakumar, P.L. Houston, and I. Burak, Phys. Rev. Lett. **56**, 1671 (1986).

[29] K.M. Chen, D.J. Tanno, and D.G. Imre, J. Phys. Chem. **101**, 2525 (1997).

[30] L.D.A. Siebbeles, M. Glass-Maujean, O.S. Vasyutinskii, J.A. Beswick, and O. Roncero, J. Chem. Phys. **100**, 3610 (1994).

[31] A.C. Kummel, G.O. Sitz, and R.N. Zare, J. Chem. Phys. **85**, 6874 (1986).

[32] A.C. Kummel, G.O. Sitz, and R.N. Zare, J. Chem. Phys. **88**, 6707 (1987).

[33] W. Happer, Rev. Mod. Phys. **44**, 169 (1972).

[34] The notation $\sigma_{KQ}(\theta, \phi)$ corresponds to $T_{KQ}(\Theta_k, \Phi_k)$ in Ref. [30].

[35] D.A. Varshalovich, A.N. Moskalev, and V.K. Khersonskii, *Quantum Theory of Angular Momentum*, World Scientific, Singapore, 1988.

[36] E.B. Alexandrov, M.P. Chaika, and G.I. Khvostenko, *Interference of atomic states*, Springer, Berlin, 1993.
[37] M. Auzinsh and R. Ferber, *Optical Polarization of Molecules*, Cambridge University Press, Cambridge, 1995.
[38] The values of the polarization matrix elements $\Phi_{kq}(\mathbf{e}) \equiv (-1)^{k+1} E_{kq}(\mathbf{e})$ for different light polarizations are also given in Ref. [15].
[39] J. Vigué, P. Grangier, G. Roger, and A. Aspect, J. Physique Lett. **42**, L531 (1981).
[40] M. Glass-Maujean and J.A. Beswick, J. Chem. Soc. Faraday Trans. **85**, 983 (1989).
[41] E.E. Nikitin and S.Y. Umanskii, *Theory of Slow Atomic Collisions*, Springer, Berlin, 1984.
[42] The Coriolis ($\Delta\Omega = \pm 1$) nonadiabatic transitions are neglected in this paper because their contribution to the photofragment polarization produced through direct dissociation processes is typically small [15].
[43] U. Fano and J.H. Macek, Rev. Mod. Phys. **45**, 553 (1973).
[44] R.N. Zare, Mol. Photochem. **4**, 1 (1972).
[45] We use here the notation β_0 instead of the more commonly used β to emphasize that this anisotropy parameter describes the angular distribution of the zeroth-order state multipole.
[46] M.P. Docker, Chem. Phys. **125**, 185 (1988).
[47] We can neglect the influence of the Cl atom nuclear spin and describe only its electron angular momentum because the dissociation occurs typically on a much faster time scale than the hyperfine interaction.
[48] A.J. Bain and A.J. McCaffery, Chem. Phys. Lett. **108**, 275 (1984).
[49] R.L. Dubs, V. McKoy, and S.N. Dixit, J. Chem. Phys. **88**, 968 (1988).
[50] R.N. Strickland and D.W. Chandler, Appl. Opt. **30**, 1811 (1991).
[51] Using the coordinate frame given in Fig. 5, the relationship between the three-dimensional intensity distribution $f(\theta,\phi)g(r)$ [52] and the image $I(\rho,\phi)$ can be written as an integral over z, $M(\rho,\phi) = \int_{-\infty}^{\infty} f(\arcsin(\rho/r),\phi)g(r)dz$, where $r^2 = \rho^2 + z^2$. Assuming that the function f is symmetric relative to reflection in the X–Y plane and substituting the integration variable z for r, one obtains Eq. (35).
[52] Most analyses of **v**–**J** correlation data assume the separability $h(r,\theta,\phi)=f(\theta,\phi)g(r)$. However in general, angular momentum polarization will depend on recoil speed, so this separation will not be valid.
[53] G.E. Busch, R.T. Mahoney, R.I. Morse, and K.R. Wilson, J. Chem. Phys. **51**, 449 (1969).
[54] R.W. Diesen, J.C. Wahr, and S.E. Adler, J. Chem. Phys. **50**, 3635 (1969).
[55] L. Li, R.J. Lipert, J. Lobue, W.A. Chupka, and S.D. Wilson, Chem. Phys. Lett. **151**, 335 (1988).
[56] Y. Matsumi, K. Tonokura, and M. Kawasaki, J. Chem. Phys. **97**, 1065 (1992).
[57] P.C. Samartzis, I. Sakellariou, T. Gougousi, and T.N. Kitsopoulos, J. Chem. Phys. **107**, 43 (1997).
[58] T.P. Rakitzis and R.N. Zare, Private communication (1998).
[59] S.D. Peyerimhoff and R.J. Buenker, Chem. Phys. **57**, 279 (1981).
[60] E.P. Gordeev, S.Ya. Umansky, and A.I. Voronin, Chem. Phys. Lett. **44**, 36 (1976).
[61] M. Saute, B. Bussery, and M. Aubert-Frécon, Mol. Phys. **51**, 1459 (1984).

[62] T. Ishiwata, A. Ishiguro, and K. Obi, J. Molec. Spec. **147**, 300 (1991).
[63] B.J. Whitaker, in R.G. Compton and G. Hancock, editors, *Research in Chemical Kinetics*, volume 1, pp. 307–346, Elsevier, Amsterdam, 1994.
[64] S. Arepalli, N. Presser, D. Robie, and R.J. Gordon, Chem. Phys. Lett. **118**, 88 (1985).
[65] A.T.J.B. Eppink and D.H. Parker, Rev. Sci. Instr. **68**, 3477 (1997).
[66] A.J. Orr-Ewing and R.N. Zare, Annu. Rev. Phys. Chem. **45**, 315 (1994).
[67] Since the precession time associated with the hyperfine structure splitting in chlorine is short with respect to the laser pulse time, we can use the long-time-limit hyperfine depolarization coefficient [1,66] which in this case evaluates to 3.7.
[68] W.H. Press, S.A. Teukolsky, W.T. Vetterling, and B.P. Flannery, *Numerical Recipes in C*, Cambridge University Press, Cambridge, 2nd edition, 1992.
[69] Strictly speaking, the matrix elements $N_{n\Omega\ n'\Omega'}^{n_e\Omega\ n'_e\Omega'}$ should be considered phenomenological parameters, since Eq. (2) was derived in the axial recoil approximation. Thus the molecular wavefunction phase difference, which is probably resposible for the sign of the observed experimental signal, was not accounted for.

TABLES

TABLE I. Alignment anisotropy parameters obtained from an SVD fit to ion image data, for the $^2S^o_{1/2}$ and $^2D^o_{5/2}$ REMPI states. The digits in parentheses are the one-standard-deviation uncertainty in the last digits of the given value. The theoretical range and interpretation of the alignment parameters is also tabulated.

Parameter	Best fit value			Range	Interpretation
	$^2S^o_{1/2}$	$^2D^o_{5/2}$	average		
s_2	−0.065(2)	−0.082(3)	−0.074(9)	−0.16...0.16	incoherent parallel and perpendicular
α_2	−0.030(2)	−0.035(2)	−0.032(3)	−0.08...0.08	incoherent parallel and perpendicular
η_2	0.094(7)	0.057(8)	0.075(20)	−0.30...0.30	coherent perpendicular
γ_2	0.014(8)	−0.013(3)	0.001(16)	−0.15...0.15	coherent parallel and perpendicular
s_2/α_2	2.2(2)	2.3(2)	2.3(3)	−1...2	
$\langle A_{20}\rangle$	−0.16(3)	−0.02(7)	−0.09(8)	−0.8...0.8	$-2(\alpha_2+\gamma_2+\eta_2)$

FIGURES

FIG. 1. Space-fixed reference frame for a diatomic molecule AB.

FIG. 2. Components of the angular distribution of electron density, associated with each state multipole ρ_{KQ}^{mol}. On the right is the distribution for a pure perpendicular transition, using α_2 and η_2 obtained for chlorine (Table I), Eq. (18) of this paper, and Eq. (4.6.21) of Ref. [1]. For the pure transition, this shape does not depend on recoil angle.

FIG. 3. Schematic of experimental apparatus. The Cartesian axis definition in this figure is used throughout the paper.

FIG. 4. Schematic potential energy curves of the chlorine molecule. The inset shows asymptotic state labels used in Sec. V.

FIG. 5. Clarification of variables in 3D to 2D transformation [Eq. (35)]. The Z axis is parallel to the axis of the TOF tube.

FIG. 6. (color) Alignment image basis functions: plots of $M_Z(t,\phi) - M_Y(t,\phi)$ [Eqs (36) and (37)] for dissociation polarization Geometries I and II. The linestrength factor ratio P_2/P_0 was not included, so that these basis images are independent of the particular probe transition. For display purposes, each image has been normalized independently. Cases (a)–(d) correspond to the following mechanistic limits: (a) incoherent perpendicular excitation, (b) incoherent parallel excitation, (c) coherent perpendicular excitation, (d) coherent parallel and perpendicular excitation. The corresponding values of the alignment anisotropy parameters are discussed in the text. Blue, red, and white correspond to positive, negative, and zero values, respectively.

FIG. 7. (color) Photofragment ion images of $Cl(^2P_{3/2}^o)$ atoms from the dissociation of chlorine molecules. The top half contains images for the $^2S_{1/2}^o$ probe state, the bottom half those for the $^2D_{5/2}^o$ state. Geometries I and II correspond to the dissociation laser parallel and perpendicular to the detector flight axis (Z), respectively. The probe laser was polarized along either the Y or Z axis.

FIG. 8. (color) Comparison of difference images (alignment images) obtained for geometries I and II with results of simulations. The top half contains images for the $^2S_{1/2}^o$ probe state, the bottom half those for the $^2D_{5/2}^o$ state. The first and third rows contain the experimental data, the second and fourth rows the simulated images. These simulations were obtained by an SVD fit using the four basis images of Fig. 6, which yielded the values listed in Table I (fourth column).

FIG. 9. Possibilities for nonadiabatic transitions for incoherent (a)–(c) and coherent (d)–(f) excitation. Note that case (c) results in coherence after a nonadiabatic transition. Only cases (a) and (f) produce photofragment alignment.

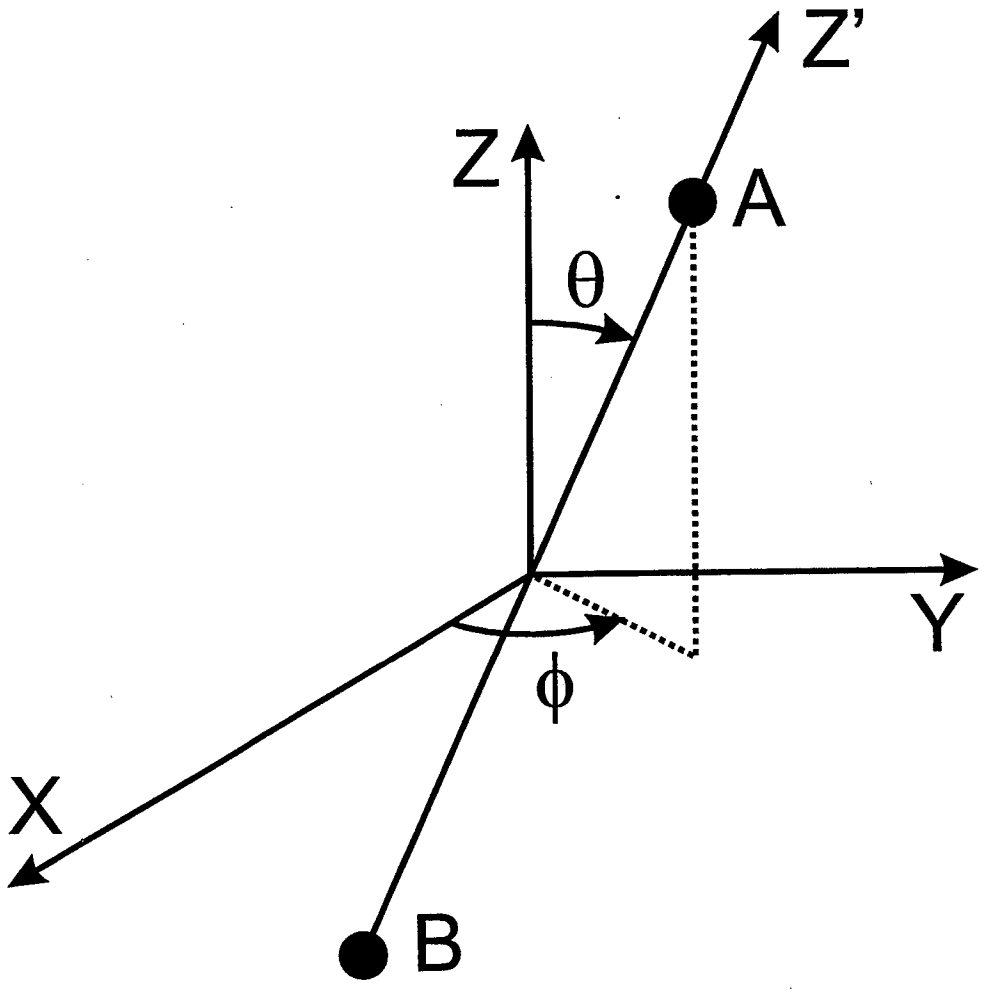

Fig. 1 Bracker et al.
Submitted to
the Journal of Chemical Physics

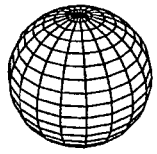

ρ_{00}^{mol}

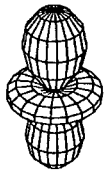

ρ_{20}^{mol}

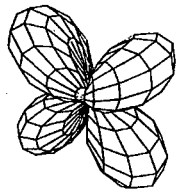

Re ρ_{21}^{mol}

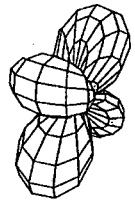

Im ρ_{21}^{mol}

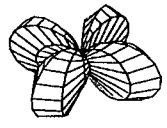

ρ_{22}^{mol}

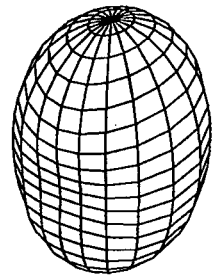

Cl

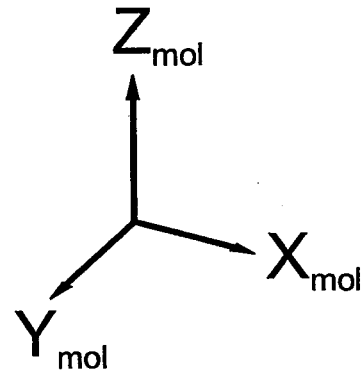

Fig. 2 Bracker et al.
Submitted to
the Journal of Chemical Physics

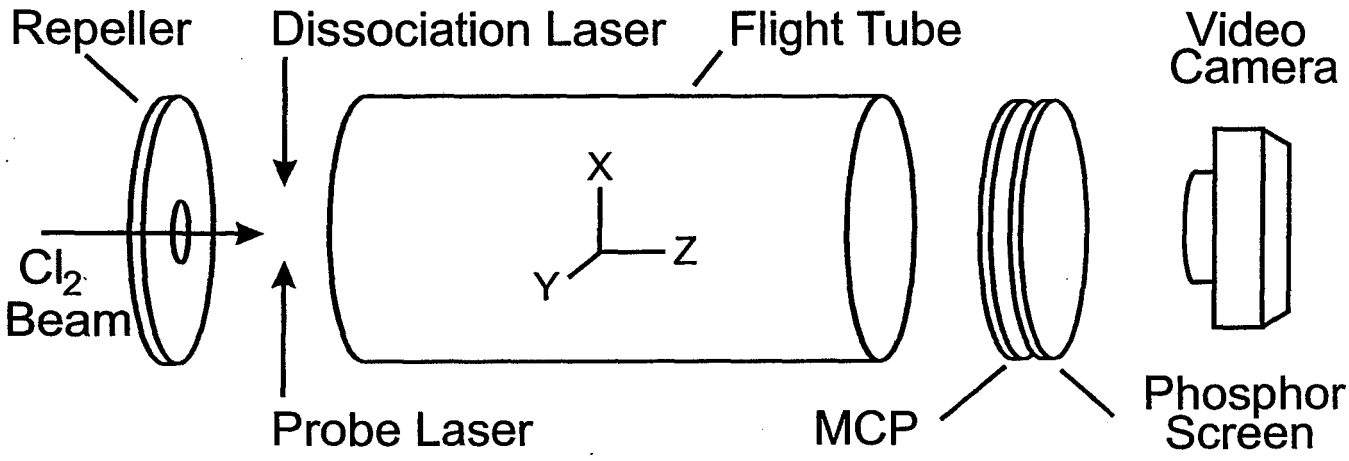

Fig. 3 Bracker et al.
Submitted to
the Journal of Chemical Physics

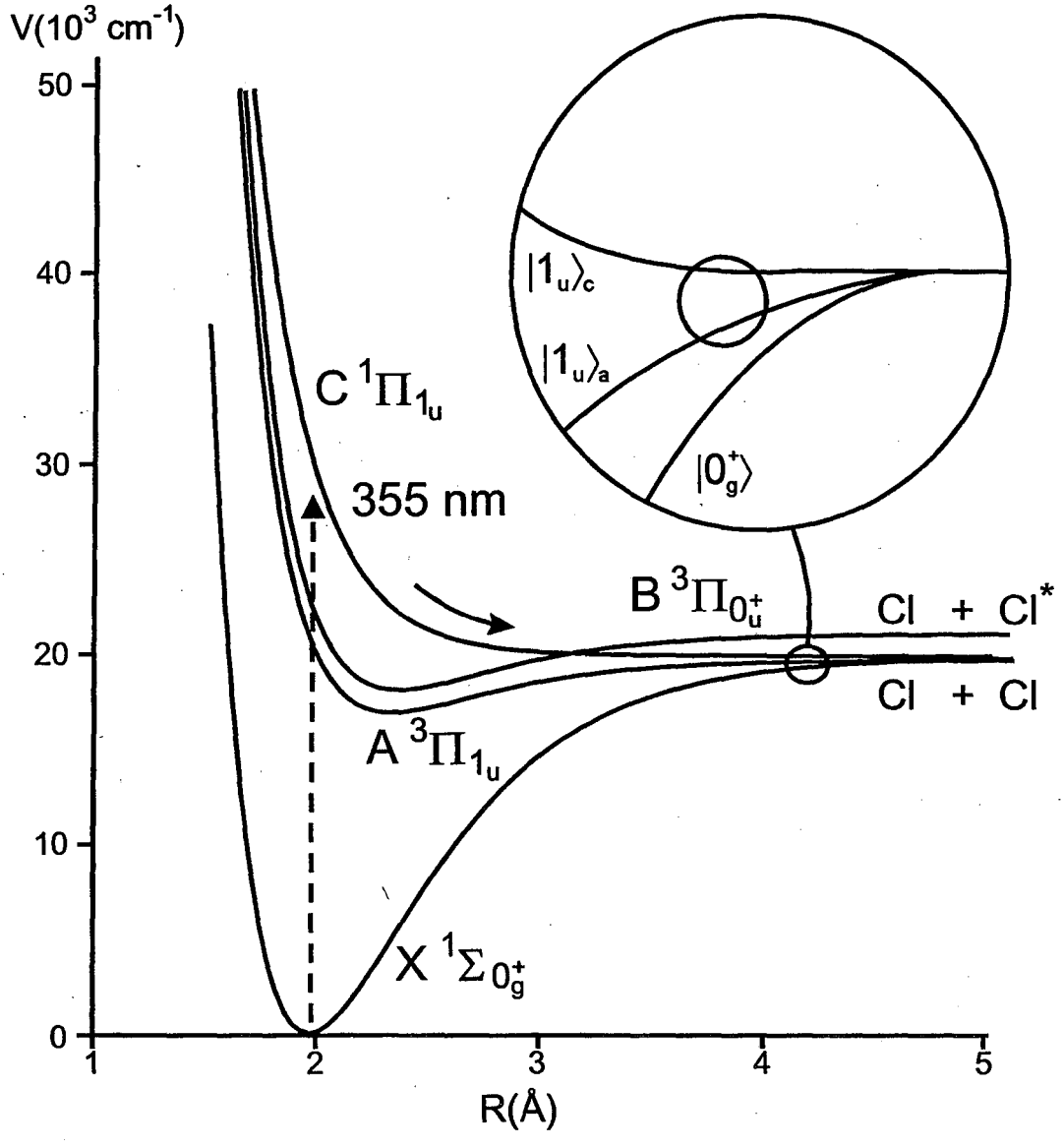

Fig. 4 Bracker et al.
Submitted to
the Journal of Chemical Physics

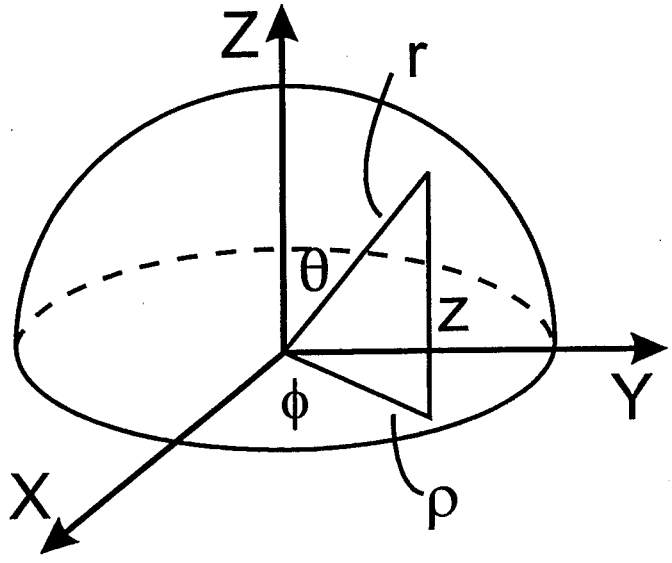

Fig. 5 Bracker et al.
Submitted to
the Journal of Chemical Physics

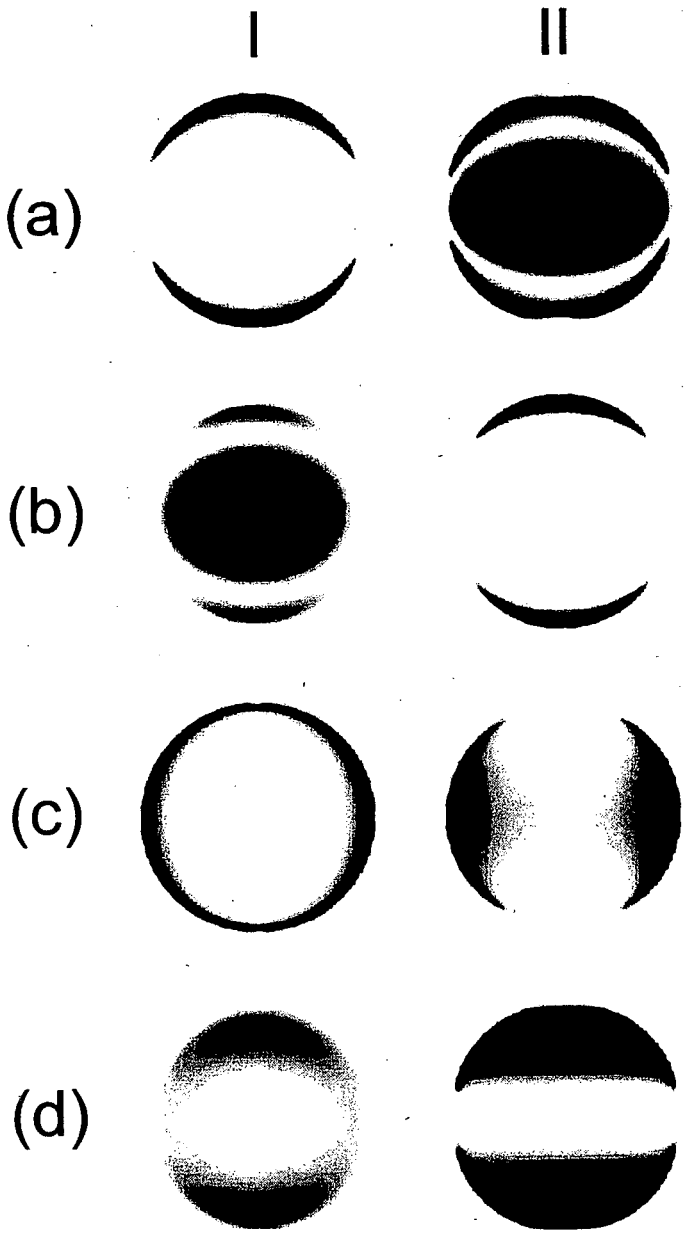

Fig. 6 Bracker et al.
Submitted to
the Journal of Chemical Physics

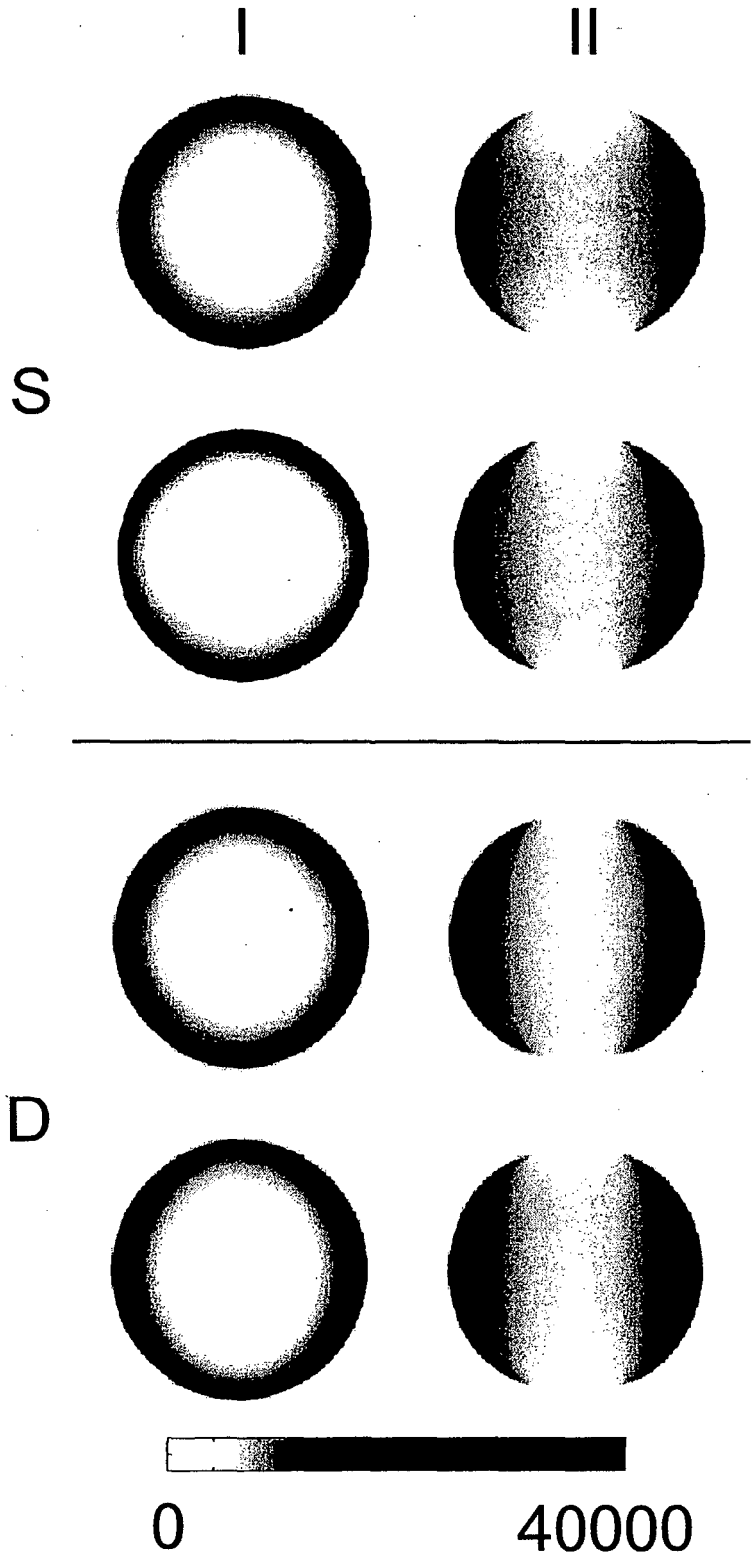

Fig. 7 Bracker et al.
Submitted to
the Journal of Chemical Physics

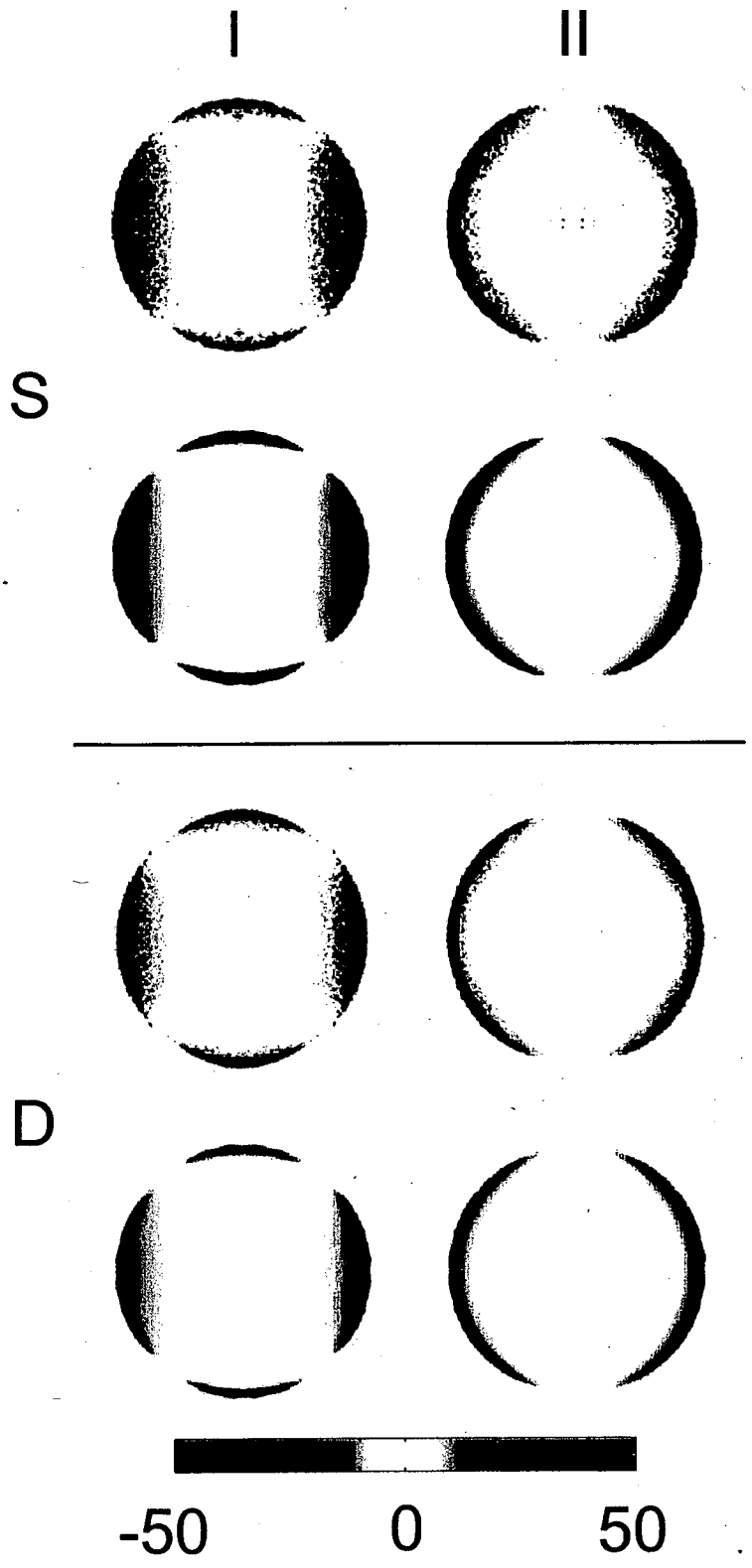

Fig. 8 Bracker et al.
Submitted to
the Journal of Chemical Physics

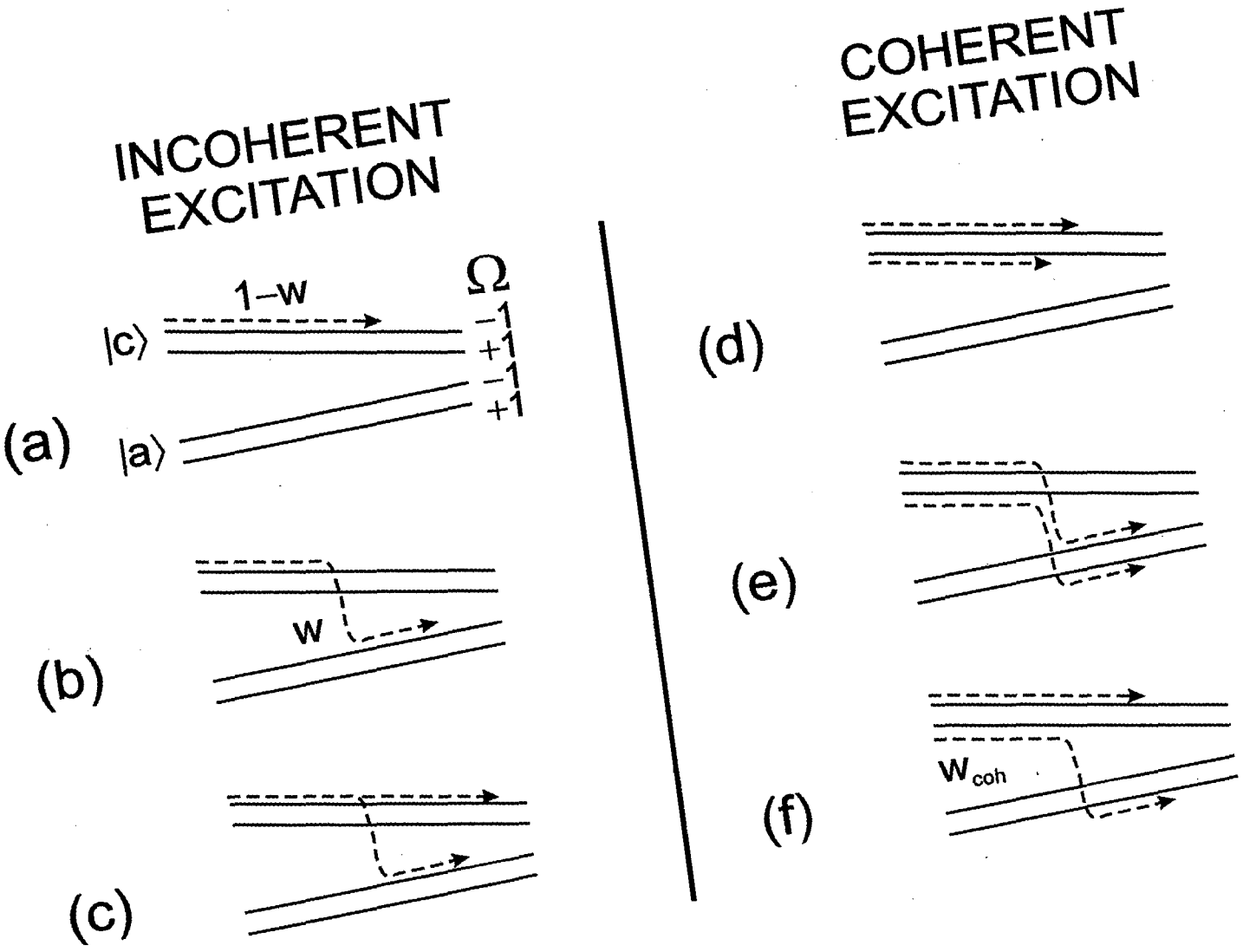

Fig. 9 Bracker et al.
Submitted to
the Journal of Chemical Physics

ERNEST ORLANDO LAWRENCE BERKELEY NATIONAL LABORATORY
ONE CYCLOTRON ROAD | BERKELEY, CALIFORNIA 94720

Prepared for the U.S. Department of Energy under Contract No. DE-AC03-76SF00098